ACS Catalysis

pubs.acs.org/acscatalysis

Research Article

Enhanced Oxygenates Formation in the Fischer–Tropsch Synthesis over Co- and/or Ni-Containing Fe Alloys: Characterization and 2D Gas Chromatographic Product Analysis

Mohamed I. Fadlalla, Sundaram Ganesh Babu, Thulani M. Nyathi, C. J. Kees-Jan Weststrate, Nico Fischer, J. W. Hans Niemantsverdriet, and Michael Claeys*

Cite This: ACS Catal. 2020, 10, 14661–14677

Read Online

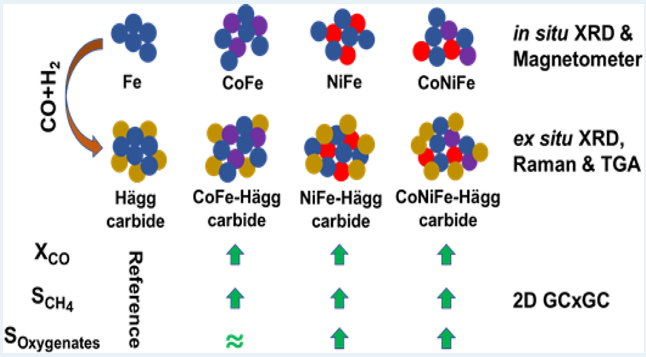

ABSTRACT: Transition metal alloys are receiving considerable attention in heterogeneous catalysis as they hold promise to combine advantageous properties of the constituting metals and, therefore, provide attractive avenues for targeted catalyst design. The present study concerns the effect of Co and Ni substituents in the ferrite (Fe_3O_4) structure used as a catalyst precursor for medium-temperature Fischer–Tropsch (MTFT) synthesis, in anticipation of enhanced oxygenate selectivities. The ferrites were synthesized by co-precipitation and characterized in detail before and after exposure to MTFT conditions, employing both conventional ex situ and state of the art in situ techniques. The complex product spectrum from the MTFT was analyzed by combining off-line one-dimensional and on-line two-dimensional gas chromatography. The latter was used specifically to investigate the formation of minority species, such as oxygenates, which are often disregarded in literature. In situ XRD and magnetometry showed no notable change in the reduction behavior of the ferrites with a cobalt substituent, but substituting with Ni decreased the reduction temperature drastically from 315 to 250 °C, most likely due to the increased hydrogen dissociation activity of Ni. The activity, CO conversion, in MTFT increased in the order Fe ≪ CoFe < NiFe < CoNiFe. Incorporation of Co and Ni in the catalysts makes them less prone to deposition of inactive carbon. The addition of Ni specifically, also results in a significant shift in selectivity toward a shorter average chain length, lower olefinicity and higher water–gas shift activity. Interestingly, these shifts are paralleled by a 76% or 170% increase in C_{2+} oxygenates selectivity or yield, respectively. The increase in hydrogenation activity of substituted (i.e., Co and/or Ni) Fe-based catalysts, plays a critical role in the Fischer–Tropsch synthesis activity and selectivity to the different product classes (i.e., paraffins, olefins, and oxygenates) and the findings reported here provide valuable insights of key importance for further development and optimization of FT catalysts.

KEYWORDS: *medium-temperature Fischer–Tropsch, ferrites, alloys, GCxGC, oxygenate selectivity*

1. INTRODUCTION

The Fischer–Tropsch synthesis (FTS) is the catalytic polymerization reaction of carbon monoxide and hydrogen (i.e., syngas) to produce a broad range of valuable hydrocarbon-based products (predominantly linear paraffins and olefins, but also, for example, alcohols, aldehydes, carboxylic acids, and aromatics).[1−3] FTS is widely considered as an alternative to refining crude oil for producing conventional fuels (gasoline, diesel, and jet fuel) from various carbon-bearing feedstocks, including natural gas, coal, biomass, and even syngas from sequestered CO_2 and electrolytic H_2.[4−6] Therefore, its economic feasibility is directly related to the global oil price. To reduce the FTS process dependency on the oil price, extensive research efforts are focused on significantly increasing the selectivity of specific high economic value compounds or product classes (e.g., fuels or light olefins) and preventing/limiting catalyst deactivation.[7] One attempt to address these challenges is the use of bimetallic catalysts, mainly consisting of FTS active metals (i.e., Fe, Co and Ni), for example, Ni–Fe/TiO_2,[8,9] Ni–Fe/Al_2O_3,[10,11] Fe–Ni/SiO_2,[12] Fe–Co alloys,[13−15] Co–Fe/TiO_2,[16−19] and even trimetallic compositions.[20] Combinations of iron with noble metals such as Pt, Ir, and Pd generally convert syngas to methanol,[21−25] while the combination of iron and rhodium is known to produce C_2 oxygenates as well.[24] Higher CO

Received: July 31, 2020
Revised: November 16, 2020

conversion was observed with the bimetallic Ni−Fe catalyst in comparison to the monometallic (i.e., Fe or Ni) catalysts for both supported and unsupported systems.[8,9,26−28] Moreover, the ratio of Ni or Co to Fe influences activity (i.e., CO conversion) and selectivity. Li et al.[27] showed that an increase of Ni in the unsupported Ni−Fe alloy increases the hydrogenation and methanation activity of the catalyst, while Ishihara et al.[12] reported similar trends with regard to hydrogenation, but did not find enhanced methanation activity for TiO_2 and SiO_2 supported Ni−Fe alloys. For the Co−Fe system, various studies report an increase in activity with increasing Co content.[12,16,26] In terms of selectivity, the higher Co content results in higher paraffin content and a decreased activity for the water−gas shift reaction.[16] Tihay et al.[13−15] showed a synergistic effect of the Co−Fe alloy and cobalt ferrite composite on the stability of the metallic phase and a higher olefin selectivity in the C_2−C_4 fraction. They also showed by X-ray diffraction (XRD) that the alloy phase and the spinel phase lose crystallinity under CO/H_2 and CO_2/H_2 conditions.[14]

Materials with a spinel structure (AB_2O_4) are extensively used in fields such as magnetism[29] and battery research,[30] owing to the possibility to modify their chemical and physical properties via the variation of the cations in the A and B sites. Furthermore, research on the use of spinel structures in catalysis include alkane oxidative dehydrogenation,[31,32] carbon monoxide oxidation,[33] and water−gas shift,[34] as well as the FTS.[35] For the latter, Chonco et al.[35] used ferrites to study the effect of copper as a promoter in iron-based catalysts. They highlighted the importance of the spinel and the delafossite structure ($Cu^{I+}Fe^{III+}O_2$) versus a physical mixture of CuO and α-Fe_2O_3, with the former structures showing higher activity. The authors suggested that the presence of copper in close proximity to iron limits the extent of sintering, thus, enhancing the carburization of the catalyst, resulting in a higher surface area of the active carbide phase.

Oxygenates, mainly alcohols, are currently used in a variety of industries, for example, ethanol is considered a valuable fuel alternative that is biodegradable[36] and butanol is viewed as an important intermediate in the plastic and pharmaceutical industries, while long chain alcohols are key in the surfactants industry.[37] Currently, alcohols are mainly produced via sugar fermentation[38] and the hydration of alkenes.[39] Direct conversion of syngas to alcohols is considered an attractive route, which in comparison to the aforementioned two routes, is versatile and environmentally friendly, since fewer operation units are required, which also result in lower capital and operation cost.[37] Syngas to oxygenates, mainly alcohols, was reported over catalysts based on different active metals: (i) cobalt, with an alcohol selectivity of 38 wt % over Co_2Cu at 240 °C,[40] ∼45 wt % over $Co_4MnK_{0.1}$ at 220 °C,[41] and ∼15 C% over Co/activated carbon at 220 °C;[42] (ii) molybdenum, with an alcohol selectivity of 50 C% over K-$NiMoS_2/Al_2O_3$-montmorillonite at 280 °C[43] and 32 C% at 250 °C over K-Mo_2C/TiO_2;[44] (iii) rhodium, with an ethanol selectivity of 24 C% at 240 °C over Rh/Al_2O_3;[45] and (iv) iron, with alcohol selectivity of 49 C% at 225 °C over Fe/Al_2O_3[46] and 62% at 320 °C over K-FeCu/silica.[47] The industrial FT process produces oxygenates in the range of 7−12 C%, based on the operating condition and the nature of the Fe catalyst.[48] However, the development of a catalyst(s) with higher activity, selectivity, and stability is needed for the industrial production of oxygenates (alcohols, aldehydes, ketones, and carboxylic acids) from syngas. This is only achievable through better understanding of the mechanism of oxygenates formation, the nature of the active site and catalyst structure−activity/selectivity correlation.

The present work focuses on the influence of substituents in the ferrite structure of catalyst precursors on the activity and selectivity in medium-temperature FTS, with the aim of increasing the selectivity toward oxygenates. The substituents used are cobalt, nickel, or a combination thereof. All catalysts are formed from the spinel structure, thus, eliminating any structural/support effects. Activation of the catalysts by reduction was investigated by means of in situ XRD and in situ magnetometry, while the physical properties of the catalysts were studied by means of nitrogen physisorption and transmission electron microscopy (TEM). For product analysis, we employ a combination of one- and two-dimensional gas chromatography, the latter coupled with mass spectrometry and a flame ionization detector, which greatly enhances product separation, identification, and quantification.

2. EXPERIMENTAL SECTION

2.1. Catalyst Synthesis. The catalysts were synthesized by a co-precipitation method described in detail by Arulmurugan et al.[49] The synthesis of Fe_3O_4 was carried out using near boiling solutions of Fe(III) nitrate (0.2 M, Sigma-Aldrich) and $FeCl_2$ (0.1 M, Sigma-Aldrich) as precursors. Both solutions (50 mL each) were added quickly to a near boiling NaOH solution (35.35 g in 1.3 L of deionized H_2O). The addition of the metal solutions resulted in an immediate formation of a black precipitate. The mixture was maintained at 95 °C for 1 h to allow sufficient time for the rearrangement of the hydroxide into the spinel structure. The mixture was allowed to cool to room temperature, and the precipitate was filtered (vacuum filtration) and washed with deionized water until the filtrate reached neutral pH. The product was dried in air at 120 °C overnight and subsequently characterized. The same synthesis method was followed for the preparation of the substituted ferrites, where an additional solution with the target concentration (0.03 M in 50 mL) of the substituent (nickel(II) nitrate and cobalt(II) nitrate, obtained from Sigma-Aldrich) was added, and the Fe(II) solution concentration changed to 0.07 M in 50 mL.

2.2. Catalyst Characterization. The crystal phase identification was achieved by XRD analysis of the powder sample using a Bruker D8 advance diffractometer equipped with a LYNXEYE XE detector and a Co source ($K_{\alpha 1}$ = 1.79 Å). The elemental composition in the ferrites was determined by inductively coupled plasma-optical emission spectroscopy (ICP-OES). In preparation, the samples (∼20 mg) were digested using a combination of HNO_3, $HClO_3$, and HCl/HF (4:1). The obtained solutions were subsequently diluted with deionized H_2O. A multistandard solution was prepared and used for ICP-OES calibration for the elements (Co, Ni, and Fe). The surface area and physisorption properties of the catalysts were measured at liquid nitrogen temperature with nitrogen as an absorbent in a Micromeritics TriStar instrument. Prior to analysis, the catalyst was degassed at 200 °C overnight in a Micromeritics FlowPrep 060 sample preparation unit. The Raman spectra of the catalysts were measured in a Renishaw inVia Raman spectrometer, operated with the Nutec software package, and equipped with a green laser (512 nm). The laser power and exposure time were varied to prevent

https://dx.doi.org/10.1021/acscatal.0c03346
ACS Catal. 2020, 10, 14661−14677

laser-induced phase transformation/damage. The shape and size of the catalysts particles were determined in a Tecnai FEI T20 transmission electron microscope operated with a field emission gun at 200 kV. The particles were immobilized on a carbon-coated copper grid.

The effect of the substituents on the reduction behavior of the different ferrites was investigated using an in situ XRD capillary cell, described in detail elsewhere,[50,51] mounted on a Bruker D8 advance diffractometer equipped with a Mo source ($K_{\alpha 1}$ = 0.71 Å) and a VANTEC detector. The total flow of pure hydrogen (used as the reducing gas) was set at 5 mL/min using a mass flow controller over a catalyst mass of ∼18 mg. The catalyst was heated from 50 to 450 °C at 1 °C/min with XRD patterns measured in 5 min intervals during ramping (step size = 0.018°, time/step = 0.2 s, total scan time = 4 min 24 s and 2θ range of 13−30°). Further investigation of the reduction temperature and pathway was carried out using an in situ magnetometer[52−54] (developed by UCT and SASOL, South Africa) with a magnetic field strength of up to 20 kOe or 2.0 T. The H_2 flow was 27.7 mL/min controlled with a mass flow controller and the temperature was monitored with a N-type thermocouple placed in the catalyst bed. The reduction method for 100 mg of the catalyst diluted with 400 mg SiC starts from 50 to 450 °C at a heating rate of 1 °C/min and back to 50 °C at 2 °C/min under pure H_2 flow. Magnetic measurements were taken every 5 min at 2, 0, and −2 T along the heating ramp from 50 to 450 °C to monitor the degree of reduction and during the cool down to 50 °C. The latter measurements, cool down curves, served to ascertain if nickel segregation occurred during reduction, which would show in a change of magnetization around its Curie temperature (353 °C). Magnetization versus field strength measurements (M−H) were also recorded at 50 (fresh/ferrite phase), 450 (reduced/alloy phase), and 50 °C (reduced/alloy phase at near room temperature) in 65 points between 2 and −2 T (total time 40 min). The γ value indicates the weight percentage of particles with sizes larger than the critical diameter for the superparamagnetic behavior of Fe (d_{crit} = 8 nm at room temperature[55]) and is calculated using the expression:

$$\gamma(\text{wt }\%) = \frac{2\cdot M_{rem}}{M_{sat}}\cdot 100 \qquad (1)$$

where γ is the percentage of non-superparamagnetic material, M_{rem} is the remnant (measured) magnetism, and M_{sat} is the saturation magnetism of the material at the temperature of measurement.

Note that, in this work, samples with γ values below 10 wt % are regarded as being superparamagnetic, as most of the particles would have a diameter smaller than the critical diameter for Fe. The remnant magnetization is measured in the absence of an external magnetic field (i.e., 0 T), while the saturation magnetization is determined by extrapolation beyond the maximum field strength of the magnetometer (i.e., >2 T). The magnetite phase is ferrimagnetic while metallic iron is ferromagnetic,[56] both of which can be detected using the magnetometer and can be distinguished from one another due to their different saturation magnetizations. It is worth noting that the magnitude of the magnetic moments decreases with temperature; therefore, an increase in the magnetization of oxidic iron samples with increasing temperature implies that oxidic Fe (and its substituents) is being reduced to metallic Fe (and its substituents).

Conventional H_2-temperature-programmed reduction (H_2-TPR) analysis was carried out using a Micromeritics AutoChem II 2920 instrument. The catalyst (∼100 mg) was placed in a quartz U-tube reactor and heated at a rate of 10 °C/min from 60 to 900 °C under a 50 mL/min flow of 5 vol % H_2 in Ar. The consumption of H_2 during the reduction experiment was analyzed using a thermal conductivity detector (TCD).

2.3. FTS Testing and Product Analysis. The FTS testing was carried out in a 1/2" stainless steel fixed bed reactor. All catalysts were tested following the same pretreatment and FTS conditions. A total of 300 mg (size range 50−75 μm) of the catalyst was diluted with 2 g of SiC (300 μm) and loaded in the predetermined isothermal zone of the reactor. The catalyst was then reduced at 400 °C for 5 h under a H_2 flow and cooled down to reaction temperature. FTS was carried out at 20 bar total pressure, 280 °C reaction temperature, a H_2/CO ratio of 2 and 36 mL/min of syngas and 4 mL/min of argon (internal reference). The reactor was connected to a hot catch pot (heated to 140 °C for wax collection) and a cold catch pot (cooled via a H_2O chiller to 10 °C for oil and H_2O collection). The catalyst activity (CO and H_2 conversion) and selectivity to CH_4 and CO_2 were analyzed on-line by a Varian CP 4900 micro GC-TCD equipped with three individual columns (10 and 20 m Mol Sieve 5A and 10 m Porapak Q). The light hydrocarbon fraction was sampled using the ampoule method,[57] before the cold trap. The ampoules were analyzed using a gas chromatograph (Varian GC 3900) equipped with a flame ionization detector (FID). To achieve effective separation of C_1 and C_2 species on the CP-Sil 5CB column, the GC oven was initially cooled to −55 °C with CO_2 before heating gradually to 250 °C. A detailed analysis of the gas phase was also carried out using a 2D GCxGC (LECO Pegasus 4D GC) equipped with a flame ionization detector (FID) and a time-of-flight-mass spectrometer (TOF-MS) directly connected to the reactor outlet gas after the hot trap. The system was operated in reverse phase mode, where the primary column has a polar stationary phase (Stabilwax, 30 m, 250 μm, 0.1 μm) and the secondary column a nonpolar one (RTX-5, 1.39 m, 180 μm, 0.2 μm). Modulation of the effluent from the primary column was achieved by cooling a dry N_2 gas stream with liquid nitrogen. The data analysis was performed using the TOF Chrom software package. Detailed 1D GC and 2D GCxGC methods and instrument parameters are provided in the Supporting Information (Table S1). The carbon balance for all FTS experiments was within the range of 92−95%.

2.4. Spent Catalyst Characterization. After the reaction, the reactor was cooled to 50 °C and the catalyst was passivated using 1% O_2 in N_2 at a flow of 50 mL/min.[58] XRD, Raman spectroscopy, and thermogravimetric analysis (TGA) of the spent catalysts was subsequently performed. The TGA analysis was carried out using a Thermal Analyzers Discovery SDT 650, with a 10 °C/min heating rate from 50 to 700 °C, under 50 mL/min air flow to decompose any carbonaceous compounds present on the catalyst surface and/or pores.

3. RESULTS

3.1. Catalyst Characterization. *3.1.1. Ex Situ Catalyst Characterization.* All synthesized materials, after drying, displayed the same diffraction patterns in XRD (Figure 1), which matched the reference pattern of iron ferrite (ICDD

https://dx.doi.org/10.1021/acscatal.0c03346
ACS Catal. 2020, 10, 14661−14677

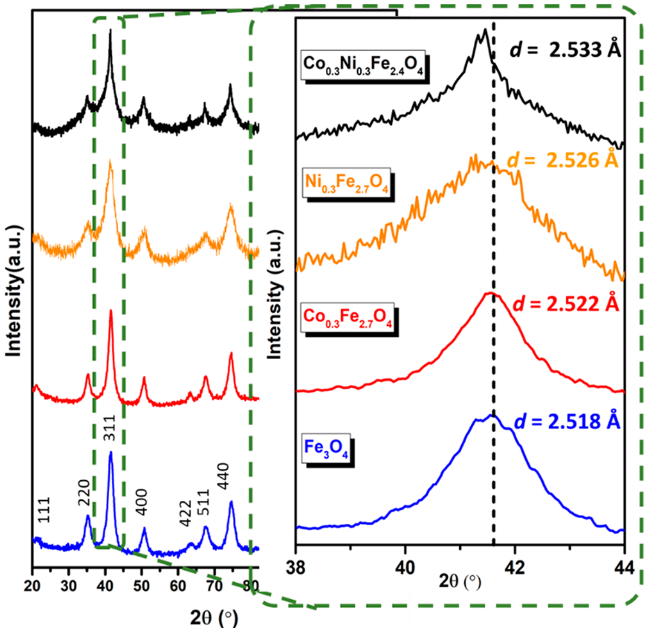

Figure 1. XRD diffraction patterns of the ferrite structures synthesized via co-precipitation, obtained with a Co source (λ = 1.79 Å). The expanded section illustrates the change in the position of the (3 1 1) reflection and *d*-spacing as a function of cation (i.e., Co, Ni, and Co−Ni) substitution in the ferrite structure.

PDF-2 entry 01−071−6336). The absence of additional diffraction lines supports the successful incorporation of the substituents into the ferrite lattice structure. Moreover, the *d*-spacing of the (3 1 1) plane, especially in the case of $Co_{0.3}Ni_{0.3}Fe_{2.4}O_4$, shifted to higher values (i.e., lower 2θ), which indicates an increase in the lattice volume due to the presence of Co and Ni. The concentration of the Co and Ni substituents was determined by ICP-OES (see Table 1). Average crystallite sizes were determined by Rietveld refinement as being 7, 7, 4, and 4 nm for Fe_3O_4, $Co_{0.3}Fe_{2.7}O_4$, $Ni_{0.3}Fe_{2.7}O_4$, and $Co_{0.3}Ni_{0.3}Fe_{2.4}O_4$, respectively. Assuming spherical particles, the theoretical crystallite sizes were calculated (see Supporting Information for calculations) using the BET surface area measurements of the different ferrites. The sizes were found to be 6, 6, 4, and 5 nm for Fe_3O_4, $Co_{0.3}Fe_{2.7}O_4$, $Ni_{0.3}Fe_{2.7}O_4$, and $Co_{0.3}Ni_{0.3}Fe_{2.4}O_4$, respectively. It is evident that there is strong concurrence between the experimental and theoretical crystallite size, where Ni-bearing ferrite demonstrated the smallest crystallite size. The same trend is qualitatively observed in the BET surface area measurements determined experimentally and theoretically (Table 1), with the highest surface areas displayed by the Ni-containing ferrites. A similar effect has previously been reported by Li et al.[27] TEM characterization indicates that all synthesized materials display irregular particle shapes (Figure 2), with no obvious alteration upon Co and/or Ni substitution.

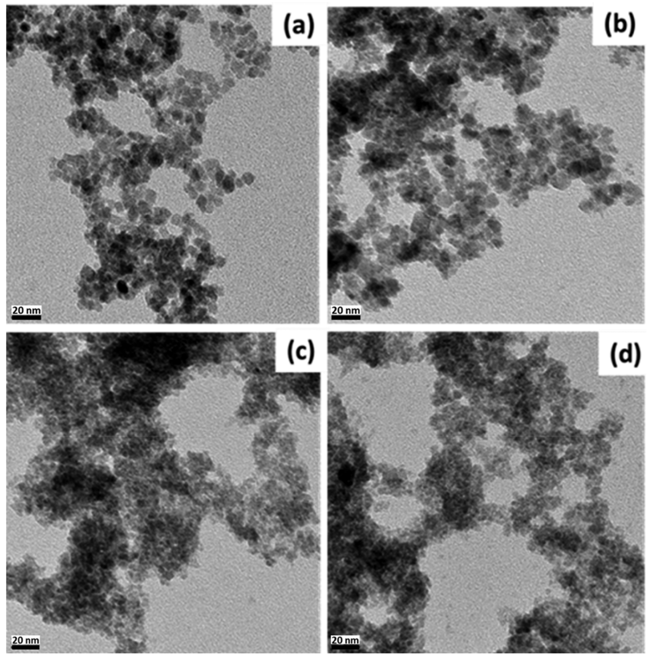

Figure 2. TEM images of ferrite and substituted ferrites synthesized via co-precipitation: Fe_3O_4 (a), $Co_{0.3}Fe_{2.7}O_4$ (b), $Ni_{0.3}Fe_{2.7}O_4$ (c), and $Co_{0.3}Ni_{0.3}Fe_{2.4}O_4$ (d).

Exceptional care must be taken when analyzing spinel-type materials with Raman spectroscopy, as the transition metal (iron, in the present case) inside the structure exhibits bivalency (ferrous or ferric).[59] A high-power laser source and long exposure under aerobic conditions can oxidize the Fe^{2+} in the spinel structure to Fe^{3+} and change the chemical and crystal phase to hematite.[59] The fingerprint vibrational stretching bands of pristine Fe_3O_4 (Figure 3) confirm the presence of the magnetite structure.[60] The Raman shifts at 350.4, 471.8, and 675.3 cm^{-1} correspond to the E_g, T_{2g}, and A_{1g} modes, respectively, which is in-line with previous reports.[61,62] The other two weak bands for the T_{2g} mode appear at 225.7 and 553.7 cm^{-1}.[61,63] The most intense band of the spectra at 675.3 cm^{-1} (for the A_{1g} mode) can be assigned to the vibration of the Fe−O bond.[61] Importantly, no notable change was observed in the Raman spectra after the incorporation of Co and/or Ni (Figure 3). This confirmed that the ferrite (spinel) crystal structure is maintained after the incorporation, which is in good agreement with the powder XRD results. The second order scattering band around 1303

Table 1. Effect of Substituents on the Ferrite Surface Area, As Determined by BET Surface Area Measurements, and the Metal Ratio in the Ferrites, As Determined by ICP-OES Analysis

catalyst	size XRD (nm)	surface area measurements (m^2 g^{-1})	theoretical surface area[a] (m^2 g^{-1})	target substituent ratio M/Fe	ICP-OES substituent ratio M/Fe
Fe_3O_4	7	183	179		
$Co_xFe_{3-x}O_4$	7	187	159	0.3/2.7	0.31/2.69
$Ni_xFe_{3-x}O_4$	4	264	290	0.3/2.7	0.30/2.70
$Ni_xCo_xFe_{3-2x}O_4$	4	251	264	0.3/0.3/2.4	0.28/0.27/2.40

[a]Assuming spherical particles with a crystallite size determined by XRD analysis (refer to Supporting Information for calculations).

https://dx.doi.org/10.1021/acscatal.0c03346
ACS Catal. 2020, 10, 14661−14677

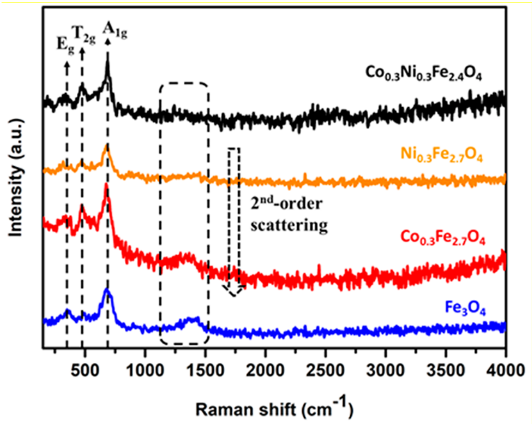

Figure 3. Raman spectra of fresh Fe_3O_4, $Co_{0.3}Fe_{2.7}O_4$, $Ni_{0.3}Fe_{2.7}O_4$, and $Co_{0.3}$ $Ni_{0.3}Fe_{2.4}O_4$ catalysts. The dotted box area highlights the 2nd order scattering band position.

cm^{-1} is a characteristic peak for iron oxide; it represents an overtone phenomenon or a combination of modes.[64] However, the incorporation of external ions masked this second order scattering, and it is almost absent in $Co_{0.3}Ni_{0.3}Fe_{2.4}O_4$.

Ex situ XRD showed similar diffraction patterns for the unsubstituted and substituted ferrites, indicating possible incorporation of the substituents in the lattice structure of the ferrite. However, this is not conclusive since XRD only detects crystalline phases. Surface area measurement by BET method showed an increase in the surface area, in particular that of the Ni-bearing ferrite. The theoretically calculated surface areas and crystallites size values were comparable with those experimentally obtained.

3.1.2. In Situ Catalyst Characterization. X-ray Diffraction. The effect of the substituents in the ferrite structure on the reduction temperature and pathway under H_2 was studied in an in-house developed in situ XRD cell.[50,51] The changes in phase composition and crystallite size were determined by Rietveld refinement using the software TOPAS 4.2[65] (using Fe_3O_4 and Fe crystal structures for refinements, with the *d* spacing allowed to vary to account for the substituents). No changes in the reduction onset temperature and reduction pathway were observed with the introduction of cobalt into the ferrite structure (Figure 4a,b). Both ferrite and cobalt ferrite have an onset reduction temperature of 315 °C and reduce to the wüstite and metal phase. In general, the reduction pathway agrees well with Ding et al.[66] The unchanged reduction temperature after inclusion of cobalt can be explained by the limited increase in the hydrogen dissociation activity of cobalt compared to iron. Cobalt-based catalysts in FTS are, therefore, commonly promoted with PGM metals to facilitate reduction.[67,68] The average crystallite size increased from 6−7 nm to 15−17 nm during reduction. It is important to note that no phase segregation was observed during reduction of the $Co_{0.3}Fe_{2.7}O_4$ phase, which suggests the presence of a CoFe alloy in the reduced phase. The latter also showed a slight increase in the *d*-spacing of the (1 1 0) plane, indicative of Co incorporation in the Fe structure.

The introduction of Ni into the ferrite structure altered the reduction behavior significantly (Figure 4a,b). The onset reduction temperature was lowered to 250 °C for both $Ni_{0.3}Fe_{2.7}O_4$ and $Co_{0.3}Ni_{0.3}Fe_{2.4}O_4$. We propose that the higher hydrogen dissociation capacity of Ni is responsible for this enhancement. Hydrogen can be activated on Ni sites and subsequently facilitate the reduction of adjacent Fe^{x+} in an intraparticle hydrogen spillover mechanism. This intermediate phase, wüstite or Ni/Ni+Co substituted wüstite, is completely reduced to the metallic/alloy phase at 325 °C. All samples show a similar degree of sintering upon reduction, with all resulting crystallite sizes ranging between 15 and 17 nm.

Magnetization Measurements. Magnetic properties of substituted ferrites have extensively been investigated; the influence of ferrite composition, crystallite size, shape and architecture have been reviewed by Kolhatkar et al.[69] Ferrite/magnetite (Fe_3O_4) has a ferrimagnetically ordered structure, in which in the absence of a magnetic field, the atomic layers with larger magnetic dipole moments align antiparallel with respect to those with smaller magnetic dipole moments. In contrast, metallic Fe is ferromagnetic, which differs from ferrite in that all magnetic dipole moments are equal in magnitude and are aligned parallel to each other.

Different iron phases and alloys exhibit differences in their saturation magnetization and Curie temperature, as summarized in Table 2. Therefore, magnetic properties can be used to study the reduction of the substituted ferrites to determine the influence of substituents on the reduction behavior and to confirm alloy formation. Since metallic iron has a higher saturation magnetization than the ferrite phase (i.e., Fe_3O_4),[56] the onset of reduction is recognized as the temperature where the magnetization increases. Table 2 shows that this is the case for the alloys as well. Noteworthy, the FeO phase is antiferromagnetic and thus undetectable in the magnetometer. However, the formation of a FeO phase (un/substituted) may otherwise be observed by a drop in the magnetization during the reduction process. This was clearly observed in the case of Fe_3O_4 and $Co_{0.3}Fe_{2.7}O_4$ by the drop in magnetization around 250 °C and to lesser extent for the Ni-bearing ferrites.

The substituents in the ferrite structure influence the magnetization of the iron-based structure, with a slight increase in magnetization upon inclusion of cobalt (from 70 to 80 emu/g) and a decrease with the inclusion of Ni (from 70 to 39 emu/g). The comparable magnetization of ferrite and cobalt ferrite and a decrease in the magnetization over nickel ferrite was also observed by Lee et al.[70] and rationalized by the change in the magnitude of the magnetic moment upon inclusion of the substituents. In general, the saturation magnetization values obtained in this study are comparable with the reported literature values (see Table 2). The differences may be due to the analysis temperature, material composition, and/or particle size.[69]

The magnetic measurements (Figure 5a) show that the onset reduction temperatures from the ferrite phase to metallic phase are about 310, 300, 245, and 260 °C, over Fe_3O_4, $Co_{0.3}Fe_{2.7}O_4$, $Ni_{0.3}Fe_{2.7}O_4$, and $Co_{0.3}Ni_{0.3}Fe_{2.4}O_4$, respectively. While these onset of reduction temperatures are in reasonable agreement with those from the XRD analysis, we note that the values obtained from the magnetic measurements are systematically lower. The reason is that XRD detects only crystalline phases, while in principle all metal ions can contribute to the magnetization and be detected with this technique. Hence, if reduction of the oxide phase initially forms unordered intermediates, these contribute to the overall magnetism, but not to the XRD.

It is important to note that both the in situ XRD and the magnetic measurements show complete reduction of the ferrites to the metallic phases, since (1) no other crystalline phases were detected besides the metallic phase in XRD, and

https://dx.doi.org/10.1021/acscatal.0c03346
ACS Catal. 2020, 10, 14661−14677

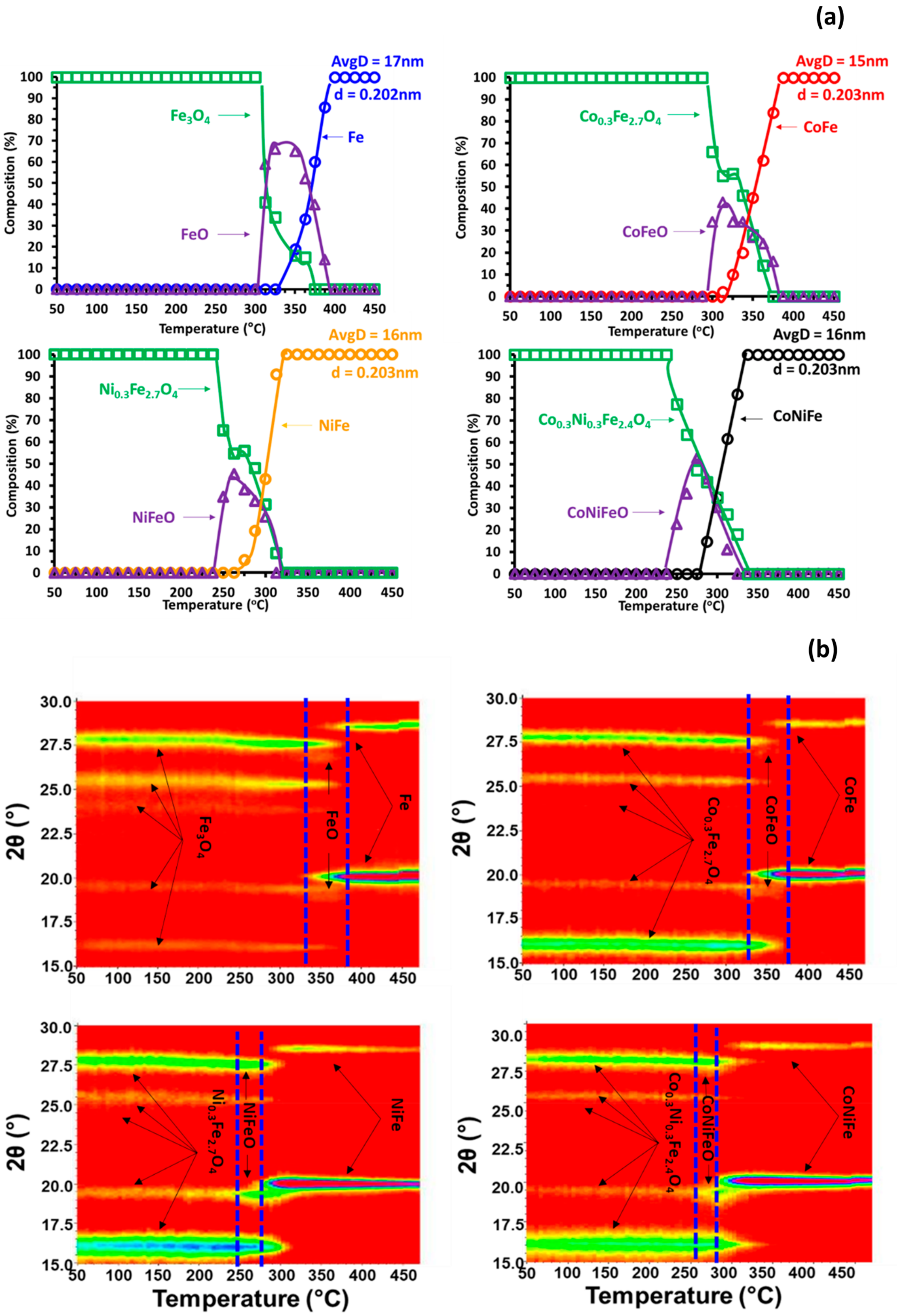

Figure 4. Compositional changes of different ferrite structures (a) and an on-top view of the XRD patterns (b) obtained in situ during H_2 reduction (XRD: Mo $K_{\alpha 1}$ = 0.71 Å).

(2) the magnetization of all catalysts reached a stable value just above the temperatures where, according to XRD, full reduction was reached. The slight decrease in magnetization toward higher temperatures is due to thermal effects.[69]

The magnetization versus field strength measurements (M–H) were used to determine the magnetic nature of the particles present in each sample, that is, whether superparamagnetic or non-superparamagnetic. The M–H measurements of Figure 5b, obtained at 450 °C, show hysteresis behavior when the applied magnetic field approaches 0, depending on the metallic phase composition. Ni-containing samples show the highest contents of superparamagnetic material, indicated by the

Table 2. Magnetic Properties of Relevant Iron Phases, Substituted Ferrites, Cobalt, Nickel and Iron Alloys

	magnetism	Curie temperature (°C)	saturation magnetism (emu g^{-1}), this study[a]	saturation magnetism (emu g^{-1}), literature	ref
α-Fe	ferromagnetic	770	204	222	56
Fe_3O_4 (magnetite)	ferrimagnetic	580 ± 15	70	90−82	56
$CoFe_2O_4$	ferrimagnetic	404	80	68−72	70−72
$NiFe_2O_4$	ferrimagnetic	517−570	39	55	73
FeO	antiferromagnetic				
$Co_{0.3}Ni_{0.3}Fe_{2.4}O_4$[a]			48		
Co		1115			74
Ni	ferromagnetic	353−358		53	74
CoFe	ferromagnetic		213	209−222	72
$Ni_{20}Fe_{80}$	ferromagnetic		173	186	75
CoNiFe[a]			189		

[a]Saturation magnetization determined in this study at 50 °C before and after reduction for the (un)substituted ferrite and iron metallic/alloy phase, respectively.

lowest γ values of 20.5 and 10.3 wt % for NiFe and CoNiFe, respectively, compared with values of 39.5 and 49.2 wt % of non-superparamagnetic material in the Fe and CoFe samples, respectively. The small hysteresis and, consequently, the low γ-values for Ni-containing alloys can be ascribed to the large Ni critical diameter of 55 nm.[69]

Magnetic measurements have been previously used to confirm alloy formation in CoNi catalysts.[74] In the case of alloy formation, the decrease in magnetization with an increase in temperature is monotonic, and no significant variation/inflection point in the absolute first derivative curve around the Ni Curie temperature region should be observed (i.e., ~353 °C, see Table 2). Figure 5c shows a monotonic decrease in magnetization with an increase in the temperature and no inflection point in the absolute first derivative curve (Figure 5d). Thus, the $Ni_{0.3}Fe_{2.7}O_4$ precursor reduced to a Ni−Fe alloy structure, while the $Co_{0.3}Ni_{0.3}Fe_{2.4}O_4$ reduced to an alloy structure evidently containing Ni+Fe. Due to the high Curie temperature of cobalt (~1115 °C, see Table 2), the same analysis cannot be done for the Co-containing alloys, as only temperatures below 1000 °C can be realized using the current magnetometry setup.[52−54]

The conventional H_2-TPR of the (un)substituted ferrites (Figure S1) shows the presence of three reduction steps. The first reduction, between 200 and 350 °C, is attributed to the reduction of Fe^{3+} (in the ferrite structure) to Fe^{2+}.[76] This reduction peak is less intense and broad in the TPR profiles of the substituted ferrites, in particular, the Ni-bearing ones, and seems to have a slightly lower onset temperature for these catalysts. It has also been proposed that this peak can be due to the reduction of hematite (α-Fe_2O_3) impurities in the ferrite.[77] Alternatively, these Fe_2O_3 "impurities" may be present as maghemite (γ-Fe_2O_3), which is indistinguishable from Fe_3O_4 in XRD characterization and which would explain why no phase change is observed in the in situ XRD reductions (see Figure 4), which correspond to these TPR peaks. The second reduction step, between 350 and 550 °C, is assigned to the reduction of the (un)substituted ferrite to a (un)substituted wüstite phase, and the third reduction, between 550 and 800 °C, may represent the transformation of the (un)substituted wüstite to the (mono-, bi- or tri)metallic phase.[76−78]

The use of in situ XRD and magnetometry for investigating the influence of substituents on the reduction behavior of the ferrite, forms a powerful combination since XRD cannot detect non-crystalline phases, which (as long as these are magnetic) are detected in the magnetometer. Both in situ techniques demonstrate that Ni acts as a reduction promoter, since inclusion of Ni results in a decreased onset of the reduction temperature from 310 °C (Fe_3O_4 and $Co_{0.3}Fe_{2.7}O_4$) to 250 °C ($Ni_{0.3}Fe_{2.7}O_4$ and $Co_{0.3}Ni_{0.3}Fe_{2.4}O_4$). We suggest that the effect is caused by the higher reducibility of Ni^{2+} to Ni^0, which then facilitates H_2 dissociation and subsequent migration to the adjacent iron and cobalt (via spillover), where initiation of the reduction process is known to be relatively difficult.[79]

3.2. Spent Catalyst Characterization. After the FT reaction, the catalysts were passivated and analyzed by XRD to determine their bulk crystalline phase composition (Figure 6). Rietveld refinement (Table 3) showed increases in the Hägg carbide concentration from 78 to 95−97 wt % for the multi-metallic catalysts (CoFe, NiFe, and CoNiFe) compared to the pure iron sample. This suggests either an improved carburization of the ferrite as a result of incorporating Co, Ni, and Co−Ni, or a suppression of the reoxidation behavior which would be caused by the product water under reaction conditions. Only the pure Fe sample showed an oxidic component, namely, magnetite, in the spent sample. The increase in the Hägg carbide concentration and disappearance of any iron oxide phase upon introduction of Co and/or Ni may be caused by a higher hydrogenation activity, assisting in the removal of oxygen from the catalyst surface, thus, preventing reoxidation of the carbide phase, in agreement with Unmuth et al.[80] The Hägg carbide formed from the metallic iron has similar crystallite size, but in the bi- and tri-metallic catalysts, the Hägg carbide is significantly smaller (Table 3). This could be due to cleavage of the metallic phase and/or intermediate phase crystallites prior to Hägg carbide phase formation. A similar observation was reported by Chonco et al.[35] during in situ XRD analysis of α-Fe_2O_3 activation in a carbon monoxide environment. The decrease in the crystallite size of the metallic catalysts (see Table 3) could therefore be another reason for the increase in the Hägg carbide content in the bi- and tri-metallic catalysts, since the carbon incorporation into the structure, to form Hägg carbide, readily occurs in smaller crystallites size Fe-based materials.[27,81−83]

A possible deactivation of Fe-based FTS catalysts is deposition of "coke" on the catalyst surface.[85] The passivated catalysts were characterized by TEM and TGA in air to determine the presence of carbon overlayers on the catalyst surface and the mass loss corresponding to carbon oxidation,

https://dx.doi.org/10.1021/acscatal.0c03346
ACS Catal. 2020, 10, 14661−14677

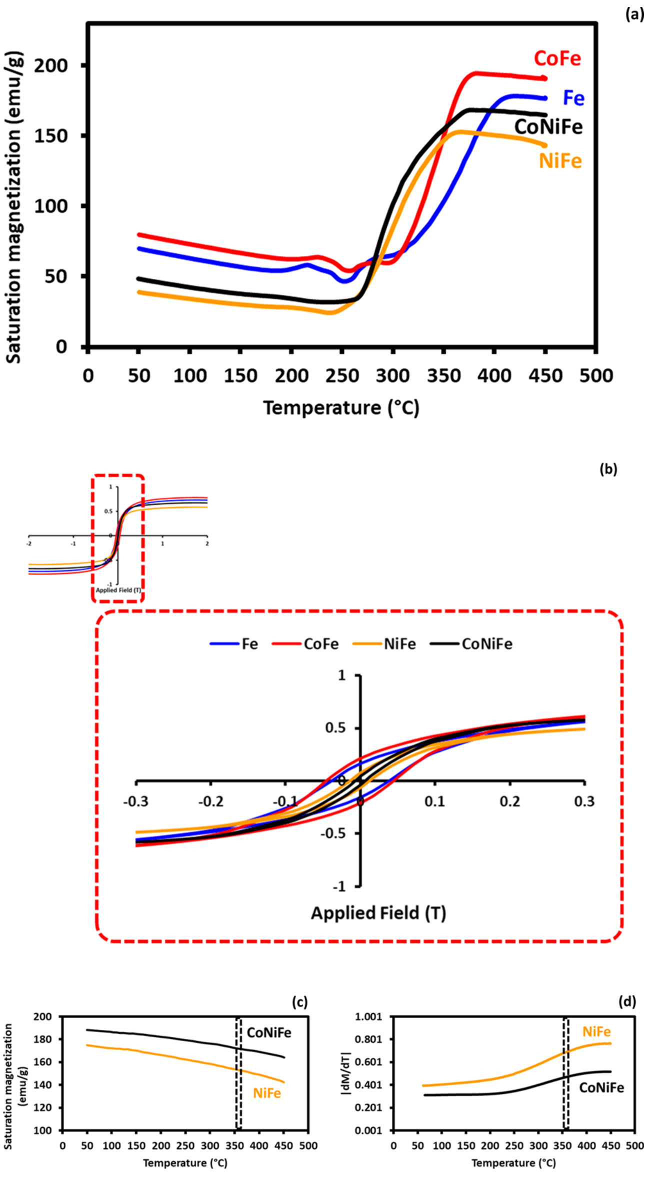

Figure 5. Saturation magnetization as a function of temperature in a H_2 environment for all catalysts (a), M−H plots obtained at 450 °C for all catalysts, with the enlarged section highlighting the hysteresis behavior (b), cooling down curves (c), and absolute first derivatives of the cooling down curves of Ni-bearing alloys (d). Dotted area in (c) and (d) indicates the Curie temperature of metallic nickel.

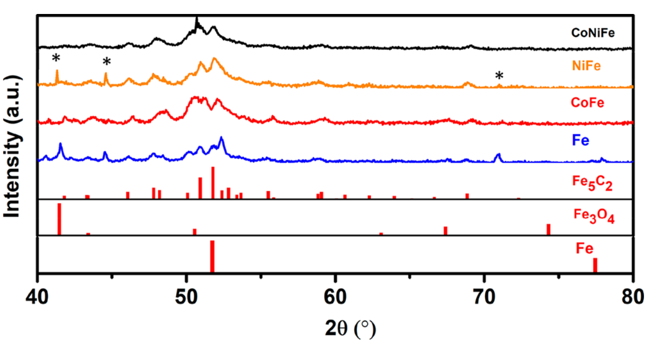

Figure 6. XRD patterns of standards and passivated spent catalysts after FTS at 280 °C, 20 bar, H_2/CO = 2. (*) Reflections due to SiC used as catalyst diluent.

respectively. Noteworthy, Hägg carbide decomposes in the same temperature range as that of "coke"; therefore, this may contribute to the mass change. However, since Hägg carbide is the dominant phase in all catalysts, the contribution will be comparable, and we assume that the main difference in the TGA profiles obtained arises from the carbon deposition. The TEM results (Figure 7) show the presence of an overlayer on (un)substituted iron catalyst particles, which is most likely due to carbon deposited during the FTS reaction. The TGA analysis (Figure 8) of the spent catalysts under air flow demonstrated mass losses of 32, 23, 14, 12 wt % from Fe, CoFe, NiFe, and CoNiFe spent catalysts, respectively. This trend is similar to that obtained for the onset reduction temperature and hydrogenation activity, where the Ni bearing alloy demonstrated the lowest onset reduction temperature and the highest hydrogenation activity. Therefore, it is possible that the hydrogen-rich catalyst surface prevents carbon deposition and/or promotes the in situ removal of carbon via hydrogenation to methane.[86,87] This could also explain the increase in methane selectivity over the Ni-bearing alloys. Furthermore, the carbonaceous material (coke) is classified in two classes, "soft" and "hard" coke. "Soft" coke consists of alkene-like compounds with an H/C ratio of 2.[88−90] These compounds decompose under an air atmosphere in the temperature range of 180−330 °C,[88] while the "hard" coke has a lower H/C ratio and decomposes in the temperature range of 300−530 °C. The mass loss for all catalysts occurs in the temperature range of 280−410 °C, possibly indicating a mixture of "soft" and "hard" coke. Hence, the substituents in the Fe catalyst only seem to influence the amount of coke formed, but not the nature of the coke formed.

The nature of carbon deposits on the catalyst surfaces, as monitored with Raman spectroscopy (Figure 9), shows a similar differentiation as the XRD analysis. The spent Fe catalyst shows two distinct bands at 1351 and 1576 cm^{-1}, which correspond to the D- and G-bands of distorted and graphitic carbon, respectively.[91−93] The other three catalysts display a broad band around 2000 cm^{-1}, suggesting the presence of amorphous carbon not coupling effectively with the laser due to very small size and low concentration of graphitic crystallites.[94,95] It appears that the deposited carbon on the alloys has a different nature to that present on the pure iron catalyst, and lacks the graphitic structure as observed on the latter. This could be a further indication of the hydrogenation activity of the substituted alloys, limiting carbon deposition and growth on the catalyst surface.

3.3. FTS Activity and Selectivity. The FTS activity (CO conversion after 48h time on stream (TOS)) of the synthesized ferrites after reduction (at 400 °C for 5 h under a flow of 100 mL/min H_2) increases with the introduction of substituents in the ferrite structure from 23.9% over Fe catalyst, to 33.6, 38.1, and 41.9%, over CoFe, NiFe, and CoNiFe, respectively (see Table 4 and Figure 10). This can be rationalized with the reported higher intrinsic CO activation capacity of Ni and Co.[2,96] The decrease in specific surface area based on the crystallite size of the reduced metal, as measured during in situ XRD, can only account for a 5−10% increase in surface atoms and can, as such, not be solely responsible for the improved activity. The CO_2 selectivity (31.1, 26.9, 35.2, and 35.0 C%, over Fe, CoFe, NiFe, and CoNiFe, respectively) decreases when Co is incorporated and increases when Ni is present. Generally, CO_2 formation in the FTS is associated with the water−gas shift (WGS) reaction,[2] with metallic iron

Table 3. Composition of Spent Catalyst (Determined via Rietveld Analysis) after 48 h TOS at 20 bar, 280 °C, H_2/CO Ratio of 2; Conversion of 24, 34, 38, and 42%, over Fe, CoFe, NiFe, and CoNiFe, Respectively

	Fe	CoFe	NiFe	CoNiFe
magnetite phase[a] (wt %)	14 (17.2 ± 1.7 nm)			
mono-/bi-/tri-metallic phase[a] (wt %)	8 (58.7 ± 5.8 nm)	5 (28.4 ± 4.1 nm)	3 (27.8 ± 8 nm)	5 (35.8 ± 6.5 nm)
Hägg carbide phase[a] (wt %)	78 (17.5 ± 0.6 nm)	95 (8.1 ± 0.2 nm)	97 (13.3 ± 0.4 nm)	95 (8.7 ± 0.3 nm)
Rwp[b] (%)	5.7	5.9	5.8	6.9

[a]Numbers in parentheses are the crystallite sizes of the phase. [b]Rwp indicates the quality of the fit obtained after applying Rietveld refinement, with values between 2 and 10% indicating a good fit.[84]

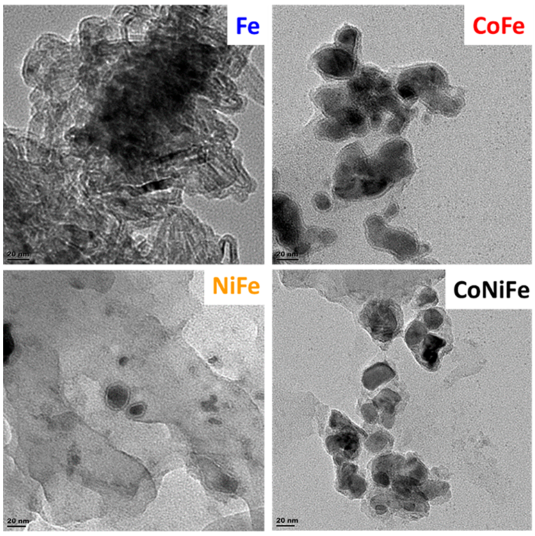

Figure 7. TEM analysis of spent and passivated catalysts after 48 h TOS at 20 bar, 280 °C, H_2/CO ratio of 2. Conversion of 24, 34, 38, and 42%, over Fe, CoFe, NiFe, and CoNiFe, respectively.

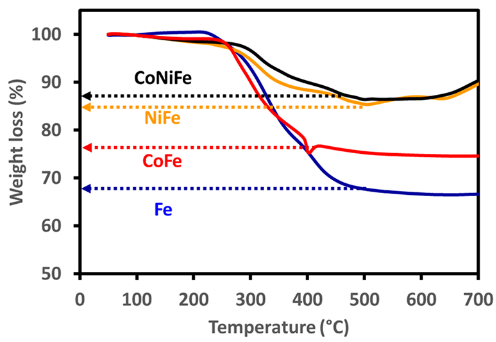

Figure 8. TGA/TPO analysis under air of passivated spent catalysts after FTS at 280 °C, 20 bar, H_2/CO = 2.

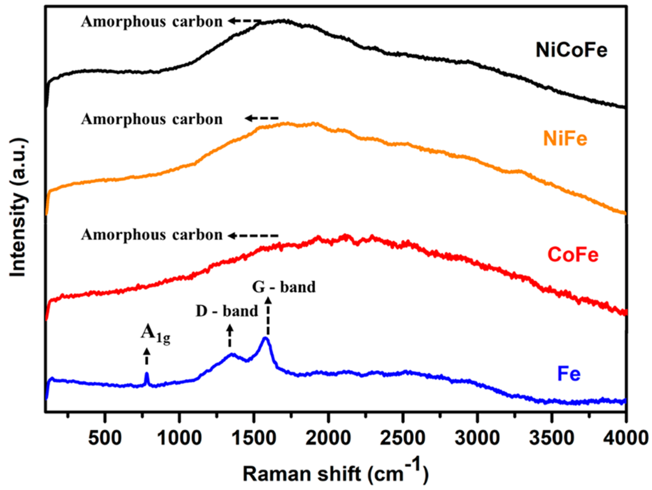

Figure 9. Raman spectra of passivated spent catalysts after FTS at 280 °C, 20 bar, H_2/CO = 2.

and the magnetite phase are well-known to sustain the WGS reaction.[2] Metallic cobalt only shows very little CO_2 selectivity under typical FTS conditions.[2,97] In the present study, it was not possible to elucidate if the observed drop in CO_2 selectivity in the presence of Co is actually based on the observed suppression of the iron oxide phase in the active catalyst (see Table 3) or through the presence of the less WGS active metallic cobalt itself. On the other hand, pure Ni has been studied as a WGS catalyst, and is usually not very effective as its CO dissociation and methanation activity dominate. Different promoting and alloying approaches have been reported to steer selectivity of Ni catalysts toward the WGS reaction, with the synthesis of NiFe alloys being one of them. It is reported that the presence of Fe weakens the strength of the CO adsorption and suppresses H_2 adsorption, overall reducing the CO dissociation/methanation activity and enhancing the WGS reaction.[98−100]

The hydrocarbon selectivity of the catalysts shows clear evidence of an increased hydrogenation activity in the presence of the substituent metals, especially Ni. The methane selectivity increases from 9.5 C% over the pure Fe catalyst, to 12.1, 30.4, and 32.5 C% over CoFe, NiFe, and CoNiFe, respectively. In parallel, the chain growth probability (C_3−C_8) decreases from 66 to 49%, again with the Ni containing samples showing the greatest change. The same effect is seen in the composition of the hydrocarbons, that is, the olefin to paraffin ratio (Table 4).

3.4. Oxygenate Formation. The detailed selectivity for the different oxygenates classes (e.g., alcohols, aldehydes, ketones, and acids) was studied with the use of 2D GC, allowing for baseline separation between the different classes of compounds based on the functional groups (i.e., paraffins, olefins, aldehydes ketones, alcohols, and acids) and the carbon number (see Figure 11), as reported by Grobler et al.[101] Since all the substituted ferrite catalysts have comparable conversion (*iso*-conversion), its effect on selectivity is assumed negligible.

The total oxygenates selectivity increased slightly by the inclusion of cobalt in the Fe catalyst (from 10.4 to 11.7 C%). Metallic cobalt is generally not regarded as highly selective toward oxygenates in the FTS.[102−104] Work reported by Gnanamani et al.[105] and Xiong et al.[106] indicates that cobalt carbide phases, potentially formed in small quantities under reaction conditions, support oxygenate formation. In the present study, there is no direct evidence of Co_2C formation, but it can also not be fully excluded. The total oxygenate selectivity increases significantly from 10.4% for iron, to 15.6−

Table 4. FTS Activity and Selectivity (given in C%) after 48 h of TOS at 20 Bar, H_2/CO Ratio of 2, and 280 °C

	Fe	CoFe	NiFe	CoNiFe
X_{CO}	23.9 ± 1.1	33.6 ± 1.6	38.1 ± 0.6	41.9 ± 1.6
α	0.66	0.64	0.49	0.49
CO_2 selectivity	31.1 ± 0.9	26.9 ± 1.0	35.2 ± 0.7	35.0 ± 0.8
selectivity to organic products				
CH_4	9.5 ± 0.1	12.1 ± 0.2	30.4 ± 0.8	32.5 ± 1.2
C_{2-4} paraffins	7.8 ± 0.8	11.5 ± 1.4	20.6 ± 0.3	18.4 ± 0.6
C_{2-4} olefins	33.9 ± 0.9	30.7 ± 1.5	20.7 ± 0.1	21.2 ± 0.2
C_{5+} paraffins	11.8 ± 0.3	11.0 ± 0.6	3.7 ± 0.2	4.2 ± 0.1
C_{5+} olefins	26.5 ± 1.1	22.7 ± 1.1	7.4 ± 0.4	7.7 ± 0.7
MeOH	0.5 ± 0.1	0.7 ± 0.1	1.2 ± 0.1	1.1 ± 0.1
C_{2+} alcohols	5.7 ± 0.9	7.8 ± 0.1	12.7 ± 0.4	11.7 ± 0.5
aldehydes	2.8 ± 0.5	2.2 ± 0.4	2.3 ± 0.4	2.2 ± 0.1
ketones	0.6 ± 0.2	0.5 ± 0.1	0.3 ± 0.06	0.7 ± 0.2
acids	0.8 ± 0.01	0.5 ± 0.01	0.5 ± 0.05	0.2 ± 0.01
$C_{3=}/C_{3-}$	5.1	2.8	3.0	3.1
primary $C_{4=}$/total $C_{4=}$	0.95	0.9	0.88	0.9

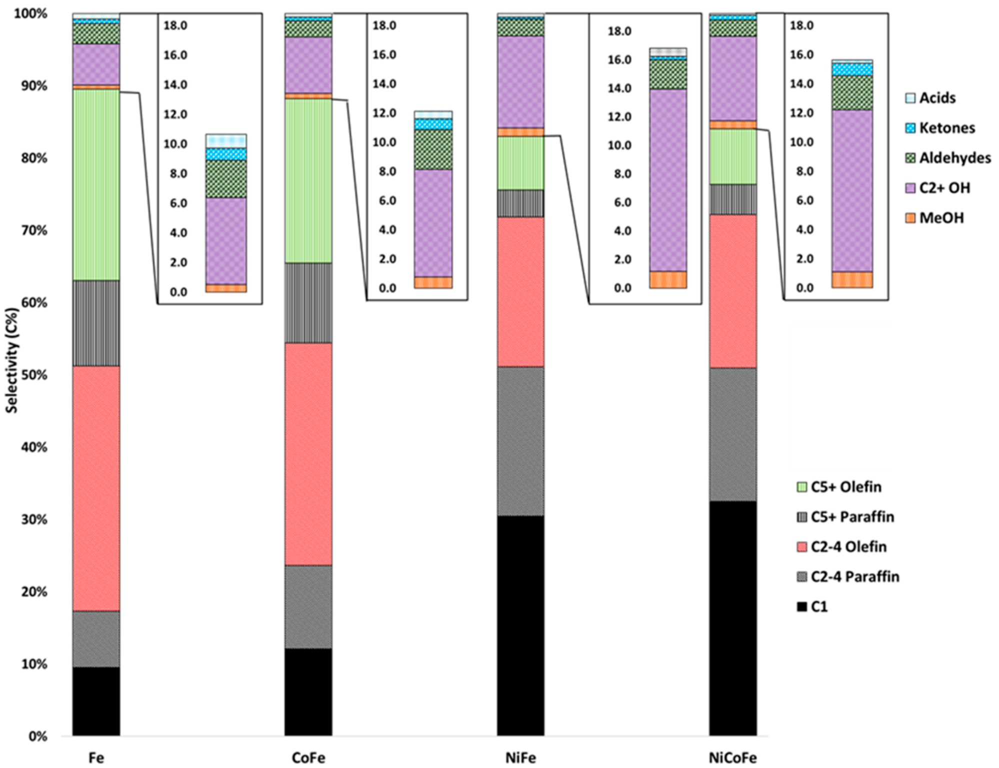

Figure 10. FTS organic product selectivity in C% after 48 h of TOS at 20 bar, H_2/CO ratio of 2, and 280 °C. Highlights show oxygenate selectivity in C%. Figure S2 (in Supporting Information) shows the selectivity, including CO_2.

16.8 C% for the Ni-containing alloys CoNiFe and NiFe. When considering the valuable C_{2+} alcohols and aldehydes only, a relative increase of up to 76% in selectivity is observed for NiFe and up to 170% improvement in yield is obtained for CoNiFe. This observation is noteworthy as oxygenates are generally believed to be prone to secondary hydrogenation reactions resulting in paraffins,[107] which one may expect to be enhanced in the presence of Ni. However, the result can be rationalized by the same hypothesis supporting an increased WGS activity, that is, the addition of Fe to Ni suppresses the hydrogen adsorption and thereby reduces the CO dissociation probability. The adsorbed molecular CO can potentially be incorporated into chain growth, yielding oxygenates, as proposed by Pichler and Schulz.[108] The increase in the oxygenate content may therefore be due to the increased formation of these primary compounds. For all catalysts, most of the oxygenates are found in the C_2 fraction, with 40−50 C% of all oxygenates. The composition of this fraction (see Figure 12a) varies greatly. In the case of the pure iron catalyst, 56.2% in the C_2 oxygenates fraction is ethanol, with the balance being made up by ethanal and acetic acid at 31.4 and 12.4%, respectively. Upon introduction of higher hydrogenation activity through incorporation of substituents, the concentration of ethanol in the C_2 oxygenates fraction increases to 76.5% in the presence of Co, and 82−84% while the catalysts contain nickel, with the acetic acid and ethanal content decrease below 4 and 20%, respectively. Overall, alcohols are the dominating oxygenate species in the product, independent

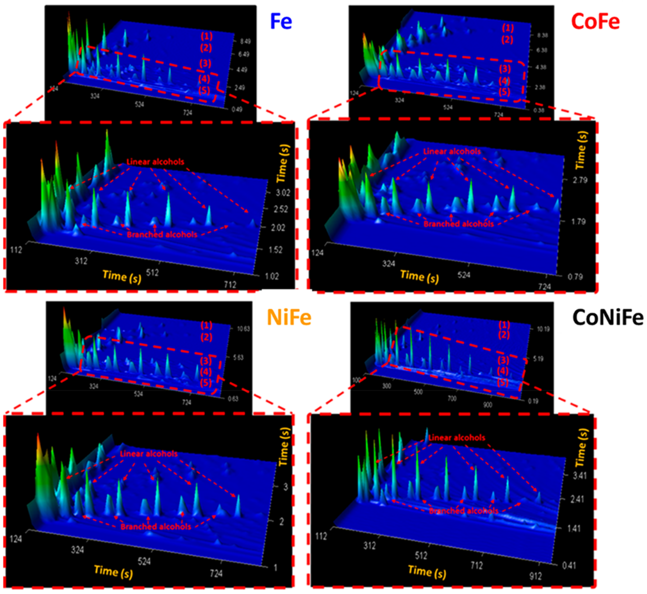

Figure 11. GCxGC-FID (logarithmic scale) online product analysis 48 h of TOS at 20 bar, H_2/CO ratio of 2, and 280 °C over Fe, CoFe, NiFe, and CoNiFe. In the small graph, (1) paraffin, (2) olefin, (3) aldehydes and ketones, (4) alcohols, and (5) acids. The enlarged sections display the retention time area of linear and branched alcohols.

of catalyst composition. Their content increases in the presence of substituents from 60% to approximately 80% of the oxygenated products. Figure 12b shows the oxygenates (i.e., alcohols, aldehydes and acids) content in the total product (i.e., oxygenate, olefin, and paraffin) with a similar carbon number. Due to the unfavored thermodynamics of methanol formation, the selectivity to this product is low. The highest selectivity was obtained at C_2, which could be due to OH addition to the CH_3−CH= catalyst surface species,[109] and/or due to the CO-insertion mechanism taking place, that is, insertion of molecular CO into the growing chain.[108] With increasing carbon number, the selectivity to oxygenates (Figure 12b) and alcohol content in total alcohols (Figure 12c) decreased, which could be rationalized by carbon number-dependent secondary conversion.[2] The ratio of linear to branched (*n*/*iso*) paraffins and alcohols (Table 5) shows similar values for the two classes of compounds (i.e., paraffins and alcohols) for each catalyst. Moreover, the inclusion of substituents (Co and/or Ni) in the Fe structure results in a drop in the normal to *iso* ratio. This correlation could be due to a common intermediate(s) for the formation of both paraffins/olefins and oxygenates.

4. DISCUSSION

Fischer−Tropsch synthesis is a well-established technology for the conversion of coal, natural gas, heavy oils, or biomass to synthetic fuels and chemicals. In the future, it is believed to play an essential role in the storage and conversion of renewable electricity as well, where CO_2 is the carbon source and electrolysis of water will provide hydrogen (and oxygen). In an eventually defossilized society, it is important to dispose over flexible carbon-neutral technology that not only provides synthetic fuels, but also a range of chemicals. Exploring how selectivities in the FTS can be manipulated by varying the composition of catalysts is therefore of great importance. The present work shows that alloying the most used FTS catalyst, iron, with other abundant metals, cobalt and nickel, provides a way to shift the product distribution toward oxygenates, with subtle but important changes in the other product classes as well.

The bi- and tri-metallic catalysts are, in fact, modified iron catalysts, derived from magnetite (ferrite) in which 10% of the

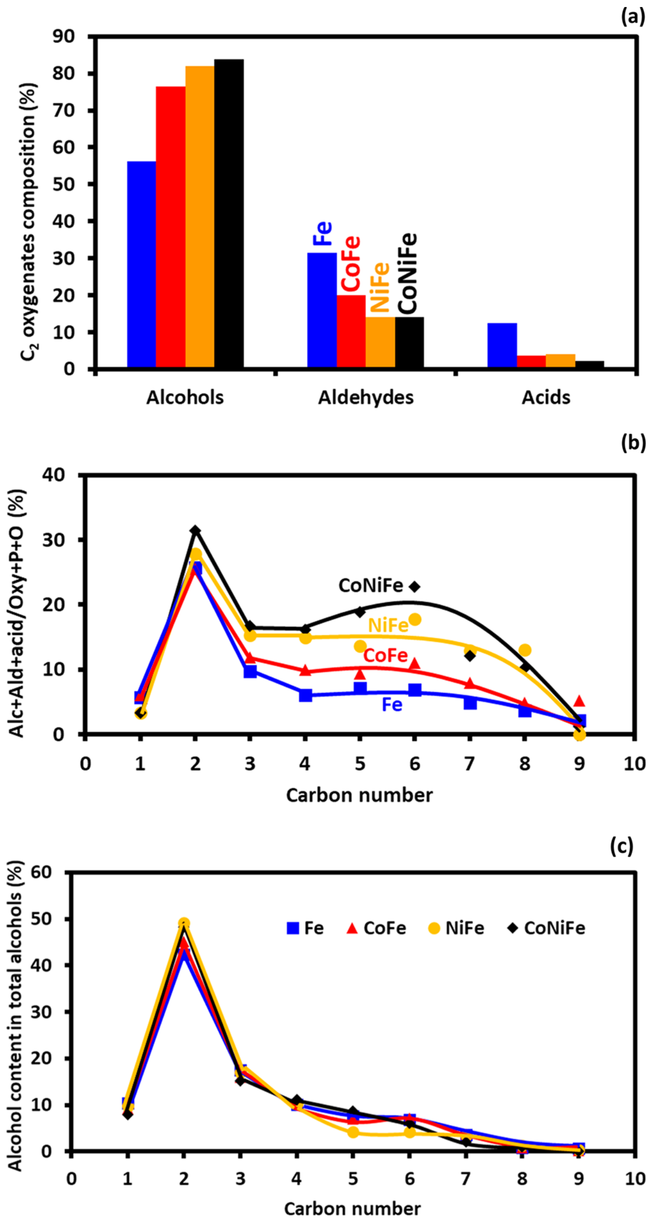

Figure 12. C_2 oxygenate composition (a), content of alcohols and aldehydes in the linear product fraction as a function of carbon number (b), and alcohol content in total alcohols as a function of carbon number (c), produced by FTS after a 48 h TOS at 280 °C, 20 bar, and H_2/CO ratio of 2.

Table 5. Linear to Branched Ratio (*n*/*iso*) in Paraffins and Alcohols after 48 h of TOS at 20 bar, H_2/CO Ratio of 2, and 280 °C, over the Four Catalysts

	Fe	CoFe	NiFe	CoNiFe
paraffins	4.2	4.1	3.5	3.6
alcohols	4.8	3.7	3.0	3.1

https://dx.doi.org/10.1021/acscatal.0c03346
ACS Catal. 2020, 10, 14661−14677

iron has been replaced by nickel or cobalt or, in the tri-metallic case, 20% by Ni and Co.

Addition of Co and/or Ni into the ferrite structure via a co-precipitation method yielded substituted ferrites with crystallite sizes ranging between 4 and 7 nm. The inclusion of the substituents in the ferrite lattice alters the position (i.e., *d*-spacing) of the (3 1 1) reflection, which is the most intense one. The XRD analysis (Figure 1) shows a slight increase in the *d*-spacing upon the introduction of the substitutes: from 2.51 Å for Fe_3O_4, to 2.52 Å for $Co_{0.3}Fe_{2.7}O_4$ and $Ni_{0.3}Fe_{2.7}O_4$, and 2.53 Å for the tri-metallic $Co_{0.3}Ni_{0.3}Fe_{2.4}O_4$. The change in *d*-spacings is small, in line with the comparable ionic radii of Fe^{2+} (0.83 Å), Co^{2+} (0.82 Å), and Ni^{2+} (0.78 Å).[110]

Also, the magnetic measurements in Table 2 indicate that the incorporation of Ni and Co in the ferrite lattice did occur, as the measured values for the saturation magnetization of the ferrite and Co-substituted ferrites were comparable, and both higher than those of the Ni-containing ferrites, in agreement with literature values. Fe_3O_4 and $CoFe_2O_4$ are reported to have similar measured magnetic moments of 4 μB,[110] while the $NiFe_2O_4$ measured magnetic moment is 2.3 μB.[110] These values explain the comparable saturation magnetization for ferrite and the Co-substituted ferrite, and both being higher than those of the Ni-containing ferrites (bi- and tri-metallic ferrite). The same effect is observed in the reduced alloys.

Hence, the characterization results are consistent with the notion that the substituting elements have indeed been incorporated in the ferrite structure. This is also reflected in the thermal evolution of the reduction process, as is clearly revealed by the in situ XRD experiments of Figure 4, and the in situ magnetization measurements of Figure 5. While the effects of cobalt incorporation in the ferrite for reduction are subtle (but noticeable, Figure 4), nickel clearly facilitates the reduction of the iron significantly and reduces the temperature needed for complete reduction by more than 50 °C.

As the Fe metal and the bi- and tri-metallic alloys exhibit higher saturation magnetization than the corresponding ferrites (Table 2), reduction can be monitored by following the magnetization in situ. One should be aware that, for superparamagnetic particles, an increase in crystallite size during the reduction process also contributes to an increase in saturation magnetization of the metallic phase. Figure 5 confirms the trend revealed by the in situ XRD that incorporation of Ni in the ferrites enhances their reducibility significantly, while Co has little effect. Reduction of oxides proceeds via the dissociation of H_2 on metallic nuclei formed at the surface of the oxide, a process that occurs more easily on nickel oxide than on iron oxide. Once such metallic nuclei have been established, H_2 molecules can dissociate readily and H-atoms can diffuse over the surface and effectuate reduction of the iron oxide. This process is often referred to as intraparticle hydrogen spillover in the literature.[79]

The iron metal and the corresponding alloys form the precursor of the catalytically active phases, which form in situ during the FTS reaction. All active samples contain the Fe_5C_2 or Hägg carbide, while it is not possible to ascertain whether these carbides contain the Co and Ni as substituents on the Fe positions or as segregated metal or carbide. Nevertheless, the effect of the substituents is obvious, in the (1) crystallite sizes of the carbide phases, which are smaller (Table 3), (2) smaller amount and different nature of the carbon accrued by the catalysts during FTS (Figures 8 and 9) and, (3) higher CO conversion levels and markedly changed product distributions during FTS.

The FTS activity of the catalysts increased in the order Fe ≪ CoFe < NiFe < CoNiFe. Several factors contribute to this trend. In addition to the larger particle size of the unpromoted iron catalyst, the degree of carburization is significantly lower than in the promoted catalysts, as the iron catalyst forms iron oxide during FTS. In contrast to this, the bi- and tri-metallic catalysts are almost fully reduced and carbided (Table 3). Furthermore, Co and Ni exhibit higher intrinsic activity than iron for CO hydrogenation.[96,111]

The product selectivity of the CoFe system resembles that of iron, but incorporation of Ni has a significant effect on the distribution of products. The NiFe and CoNiFe catalysts show higher hydrogenation activity, as evident in the higher selectivity for CH_4, a lower chain-growth probability, lower olefin/paraffin ratios in the C_{2-4} and C_{5+} fraction, and a doubling in the selectivity toward oxygenates, notably C_{2+} alcohols. It is well-known that the primary FTS product is rich in olefins, while subsequent secondary readsorption and hydrogenation enhances the overall paraffin content.[112] The olefin to paraffin ratio in the product fraction with carbon numbers of 2−4 drops from 4.3 to 2.9 when Co is incorporated into the catalyst and to 1 in the presence of Ni. The same qualitative trend is observed for the longer carbon chain numbers at an overall lower olefin content, a well-documented observation associated to a longer residence time of the primary olefin and, therefore, a higher probability of secondary hydrogenation.[112−114] The increases in the paraffin content, methane selectivity, and decreased chain growth probability upon incorporation of nickel in the catalyst can be attributed to the relatively high hydrogenation activity of nickel, and is in fact also reflected in the enhanced reducibility of the Ni-containing catalysts, as discussed above.

The oxygenate selectivities over Fe, CoFe, NiFe, and CoNiFe were 10.4, 11.7, 17.0, and 15.9 C%, respectively (Table 4 and Figure 10), the dominant oxygenates being alcohols, followed by aldehydes. Ethanol is the predominant product, representing 40−50% of all oxygenates. Within the C_2 oxygenates, the ethanol content increases from 56% on pure Fe, to 76% on CoFe and 82−84% for the Ni-containing alloys. The selectivity of valuable C_{2+} alcohols plus aldehydes increased from 8.5 to 15 C% which translates to a relative increase of 76%. This effect is even more substantial when expressing the C_{2+} oxygenates formation in terms of yields (1.40, 2.45, 3.71, 3.78 C% over Fe, CoFe, NiFe, and CoNiFe, respectively) as increases of 75, 165, and 170% were obtained via Co, Ni, and Co+Ni modification, respectively. The findings are considered to be of key importance for further development of active and selective catalysts for specific classes of compounds. It is likely that additional promotion (e.g., with alkali metals) can greatly enhance performance in terms of this type of catalysts and bring them on par with state-of-the-art catalysts for the production of oxygenates from synthesis gas.[115,116]

There are different proposed formation mechanisms for oxygenates reported in literature.[2] Aldehydes and alcohols form in the "enol" mechanism via a chain termination step, while acids may form via the Cannizzaro reaction (i.e., secondary reaction of aldehydes).[2] Johnston and Joyner[117] proposed that alcohol formation takes place via the coupling reaction of alkyl and surface hydroxyl groups. However, the most considered mechanism of oxygenate formation in FTS is

https://dx.doi.org/10.1021/acscatal.0c03346
ACS Catal. 2020, 10, 14661−14677

the CO insertion mechanism.[2,108] In this mechanism, chain growth takes place via CO insertion into a metal−alkyl group, yielding a surface acyl species. As C_1 species are believed to dominate on the catalyst surface (as also reflected in methane selectivities often larger than expected due to ideal Anderson−Schulz−Flory kinetics),[2] this predominantly leads to the formation of C_2 oxygenates (mostly ethanol), as observed in this study. The formation of paraffins and olefins occurs by termination of the growing chain through hydrogen addition or β-H-elimination, respectively. Importantly, alcohols are proposed to form via the reaction of RCHOH surface species with hydrogen. Aldehyde formation can take place via β-H-elimination of RCHOH, yielding enol species, which isomerize to aldehydes.[2] Considering the widely accepted CO insertion mechanism for higher alcohols formation, in particular, ethanol,[118,119] two types of active sites may be required to facilitate chain propagation and CO non-dissociative adsorption, as well as insertion into the growing chain. The former function is possibly carried out over the Fe sites, while the latter two functions preferably occur over the alloy sites (Co- and/or Ni-Fe site). The presence of the substituents therefore aids in the formation of oxygenates. Oxygenates are also reported to undergo secondary reactions, including hydrogenation and incorporation into the growing chain.[120−122] The high oxygenates selectivity at the C_2 position could be explained by the high stability of ethanol, in comparison to C_{3+} alcohols, against secondary reactions[123] and the possibility of ethanol forming via an additional route, to CO insertion, by the reaction of surface ethylidene with an OH group.[124] In general, the production of oxygenates, in particular, alcohols, require a catalyst that would facilitate the chain growth/propagation and CO insertion steps.[125] Although the catalytic material in this study does not provide high oxygenates selectivity, it provides a route to at least enhance oxygenates formation via a stabilized Fe-based catalyst with limited carbon deposition and improving reducibility and carburization.

Finally, we note that the GCxGC product analysis in Figure 11 illustrates how rich the product distributions of the FTS catalysts are. In the future, we intend to employ such information for detailed mechanistic studies of chain growth in the Fischer−Tropsch reaction.

5. CONCLUSION

The study determined the influence of Co and/or Ni substituents in the ferrite structure and on the chemical and physical properties, as well as FTS activity and selectivity, particularly to oxygenated compounds. Characterization via in situ XRD and magnetometry analyses under a H_2 environment showed that Ni acts as a reduction promoter by facilitating the reduction of the ferrite at lower temperatures. Alloys were formed upon reduction, but exposure to FT conditions caused the formation of Hägg carbide, likely containing Co and Ni as substituents. The modification with Co and Ni further resulted in smaller crystallites, less carbon deposition, and pronounced positive effects on FTS activity (i.e., CO conversion), as well as increased selectivities to methane, paraffins and oxygenates. It is likely that the modification, in particular that with nickel, leads to significant changes in hydrogen availability on the catalyst surface, which selectively affects steps of product formation ultimately promoting desorption as alcohols. The findings of this study are of fundamental importance toward the development of iron-based catalysts optimized for selective product formation.

■ ASSOCIATED CONTENT

Supporting Information

The Supporting Information is available free of charge at https://pubs.acs.org/doi/10.1021/acscatal.0c03346.

Theoretical calculations of the catalyst surface area and crystallite size, FTS activity and selectivity calculation/formulas, and conventional H_2-TPR profile, as well as detailed 2D GCxGC analysis method is provided (PDF)

■ AUTHOR INFORMATION

Corresponding Author

Michael Claeys − *Catalysis Institute and c*change (DSI-NRF Centre of Excellence in Catalysis), Department of Chemical Engineering, University of Cape Town, Rondebosch 7701, South Africa;* orcid.org/0000-0002-5797-5023; Email: michael.claeys@uct.ac.za

Authors

Mohamed I. Fadlalla − *Catalysis Institute and c*change (DSI-NRF Centre of Excellence in Catalysis), Department of Chemical Engineering, University of Cape Town, Rondebosch 7701, South Africa*

Sundaram Ganesh Babu − *Catalysis Institute and c*change (DSI-NRF Centre of Excellence in Catalysis), Department of Chemical Engineering, University of Cape Town, Rondebosch 7701, South Africa*

Thulani M. Nyathi − *Catalysis Institute and c*change (DSI-NRF Centre of Excellence in Catalysis), Department of Chemical Engineering, University of Cape Town, Rondebosch 7701, South Africa*

C. J. Kees-Jan Weststrate − *SynCat@DIFFER, Syngaschem BV, 5600 HH Eindhoven, The Netherlands*

Nico Fischer − *Catalysis Institute and c*change (DSI-NRF Centre of Excellence in Catalysis), Department of Chemical Engineering, University of Cape Town, Rondebosch 7701, South Africa;* orcid.org/0000-0002-8817-3621

J. W. Hans Niemantsverdriet − *Catalysis Institute and c*change (DSI-NRF Centre of Excellence in Catalysis), Department of Chemical Engineering, University of Cape Town, Rondebosch 7701, South Africa; SynCat@DIFFER, Syngaschem BV, 5600 HH Eindhoven, The Netherlands*

Complete contact information is available at: https://pubs.acs.org/10.1021/acscatal.0c03346

Notes

The authors declare no competing financial interest.

■ ACKNOWLEDGMENTS

The authors acknowledge the financial contributions from c*change (DSI-NRF Centre of Excellence in Catalysis), the National Research Foundation (NRF), and Syngaschem BV, Eindhoven, The Netherlands. The latter is grateful for funding from Synfuels China Technology Co. Ltd, Beijing-Huairou. We further acknowledge the Aaron Klug Centre for Imaging and Analysis at the University of Cape Town, Mr. Russell Geland from the analytical laboratory for ICP-OES and BET-surface area measurements, and Mr. Dominic de Oliveira and Mr. Adli Peck for assistance with the magnetometer analysis.

■ REFERENCES

(1) van der Laan, G. P.; Beenackers, A. A. C. M. Kinetics and Selectivity of the Fischer−Tropsch Synthesis: A Literature Review. *Catal. Rev.: Sci. Eng.* **1999**, *41* (3−4), 255−318.

(2) Claeys, M.; van Steen, E. Basic studies. In *Stud. Surf. Sci. Catal.*; Steynberg, A., Dry, M., Eds.; Elsevier, 2004; Vol. *152*, Chapter 8, pp 601−680.

(3) van de Loosdrecht, J.; Botes, F. G.; Ciobica, I. M.; Ferreira, A.; Gibson, P.; Moodley, D. J.; Saib, A. M.; Visagie, J. L.; Weststrate, C. J.; Niemantsverdriet, J. W. 7.20 - Fischer−Tropsch Synthesis: Catalysts and Chemistry. In *Comprehensive Inorganic Chemistry II*, 2nd ed.; Reedijk, J., Poeppelmeier, K., Eds.; Elsevier: Amsterdam, 2013; pp 525−557.

(4) Abelló, S.; Montané, D. Exploring Iron-based Multifunctional Catalysts for Fischer−Tropsch Synthesis: A Review. *ChemSusChem* **2011**, *4* (11), 1538−1556.

(5) Jahangiri, H.; Bennett, J.; Mahjoubi, P.; Wilson, K.; Gu, S. A review of advanced catalyst development for Fischer−Tropsch synthesis of hydrocarbons from biomass derived syn-gas. *Catal. Sci. Technol.* **2014**, *4* (8), 2210−2229.

(6) Sapountzi, F. M.; Gracia, J. M.; Weststrate, C. J.; Fredriksson, H. O. A.; Niemantsverdriet, J. W. Electrocatalysts for the generation of hydrogen, oxygen and synthesis gas. *Prog. Energy Combust. Sci.* **2017**, *58*, 1−35.

(7) Calderone, V. R.; Shiju, N. R.; Ferre, D. C.; Rothenberg, G. Bimetallic catalysts for the Fischer−Tropsch reaction. *Green Chem.* **2011**, *13* (8), 1950−1959.

(8) Jothimurugesan, K.; Gangwal, S. K. Titania-Supported Bimetallic Catalysts Combined with HZSM-5 for Fischer−Tropsch Synthesis. *Ind. Eng. Chem. Res.* **1998**, *37* (4), 1181−1188.

(9) van de Loosdrecht, J.; van der Kraan, A. M.; van Dillen, A. J.; Geus, J. W. Metal-support interaction: titania-supported nickel-iron catalysts. *Catal. Lett.* **1996**, *41* (1), 27−34.

(10) Feyzi, M.; Khodaei, M. M.; Shahmoradi, J. Effect of sulfur on the catalytic performance of Fe−Ni/Al_2O_3 catalysts for light olefins production. *J. Taiwan Inst. Chem. Eng.* **2014**, *45* (2), 452−460.

(11) Feyzi, M.; Mirzaei, A. A.; Bozorgzadeh, H. R. Effects of preparation and operation conditions on precipitated iron nickel catalysts for Fischer−Tropsch synthesis. *J. Nat. Gas Chem.* **2010**, *19* (3), 341−353.

(12) Ishihara, T.; Eguchi, K.; Arai, H. Hydrogenation of carbon monoxide over SiO_2-supported Fe-Co, Co-Ni and Ni-Fe bimetallic catalysts. *Appl. Catal.* **1987**, *30* (2), 225−238.

(13) Tihay, F.; Pourroy, G.; Roger, A. C.; Kiennemann, A. Selective synthesis of C_2-C_4 olefins on Fe-Co based metal/oxide composite materials. In *Stud. Surf. Sci. Catal.*; Parmaliana, A., Sanfilippo, D., Frusteri, F., Vaccari, A., Arena, F., Eds.; Elsevier, 1998; Vol. *119*, pp 143−148.

(14) Tihay, F.; Roger, A. C.; Kiennemann, A.; Pourroy, G. Fe−Co based metal/spinel to produce light olefins from syngas. *Catal. Today* **2000**, *58* (4), 263−269.

(15) Tihay, F.; Roger, A. C.; Pourroy, G.; Kiennemann, A. Role of the Alloy and Spinel in the Catalytic Behavior of Fe-Co/Cobalt Magnetite Composites under CO and CO_2 Hydrogenation. *Energy Fuels* **2002**, *16* (5), 1271−1276.

(16) Duvenhage, D. J.; Coville, N. J. Fe:Co/TiO_2 bimetallic catalysts for the Fischer−Tropsch reaction: Part 4: A study of nitrate and carbonyl derived FT catalysts. *J. Mol. Catal. A: Chem.* **2005**, *235* (1), 230−239.

(17) Duvenhage, D. J.; Coville, N. J. Fe:CoTiO_2 bimetallic catalysts for the Fischer−Tropsch reaction I. Characterization and reactor studies. *Appl. Catal., A* **1997**, *153* (1), 43−67.

(18) Duvenhage, D. J.; Coville, N. J. Fe:Co/TiO_2 bimetallic catalysts for the Fischer−Tropsch reaction: Part 2. The effect of calcination and reduction temperature. *Appl. Catal., A* **2002**, *233* (1), 63−75.

(19) Duvenhage, D. J.; Coville, N. J. Fe:Co/TiO_2 bimetallic catalysts for the Fischer−Tropsch reaction: Part 3: The effect of Fe:Co ratio, mixing and loading on FT product selectivity. *Appl. Catal., A* **2005**, *289* (2), 231−239.

(20) Azizi, H. R.; Mirzaei, A. A.; Kaykhaii, M.; Mansouri, M. Fischer−Tropsch synthesis: Studies effect of reduction variables on the performance of Fe−Ni−Co catalyst. *J. Nat. Gas Sci. Eng.* **2014**, *18*, 484−491.

(21) Niemantsverdriet, J. W.; Van Grondelle, J.; Van der Kraan, A. M. Methanol from synthesis gas over bimetallic FePd catalysts. *Hyperfine Interact.* **1988**, *41* (1), 677−680.

(22) Kimura, T.; Fukuoka, A.; Fumagalli, A.; Ichikawa, M. Fe-Promoted selective methanol synthesis in CO hydrogenation catalyzed on SiO_2-supported Ir_4Fe and Pd_6Fe_6 bimetallic carbonyl cluster-derived catalysts. *Catal. Lett.* **1989**, *2* (4), 227−233.

(23) Fukushima, T.; Araki, K.; Ichikawa, M. Promoting effects of Fe addition in MeOH synthesis catalysed by SiO_2-supported Pd. *J. Chem. Soc., Chem. Commun.* **1986**, No. 2, 148b−150.

(24) Bhasin, M. M.; Bartley, W. J.; Ellgen, P. C.; Wilson, T. P. Synthesis gas conversion over supported rhodium and rhodium-iron catalysts. *J. Catal.* **1978**, *54* (2), 120−128.

(25) van Gruijthuijsen, L. M. P.; Louwers, S. P. A.; van Santen, R. A.; Niemantsverdriet, J. W. CO bonding and hydrogenation activity of promoted noble metal catalysts during restructuring in high-pressure CO hydrogenation: FeIr/SiO_2. *Catal. Lett.* **1997**, *43* (1), 45−49.

(26) Arai, H.; Mitsuishi, K.; Seiyama, T. TiO_2-supported Fe−Co, Co−Ni, and Ni−Fe alloy catalysts for Fischer−Tropsch synthesis. *Chem. Lett.* **1984**, *13* (8), 1291−1294.

(27) Li, T.; Wang, H.; Yang, Y.; Xiang, H.; Li, Y. Study on an iron−nickel bimetallic Fischer−Tropsch synthesis catalyst. *Fuel Process. Technol.* **2014**, *118*, 117−124.

(28) Cooper, M. E.; Frost, J. New iron/nickel alloy catalyst for Fischer−Tropsch synthesis. *Appl. Catal.* **1990**, *57* (1), L5−L8.

(29) Modak, S.; Ammar, M.; Mazaleyrat, F.; Das, S.; Chakrabarti, P. K. XRD, HRTEM and magnetic properties of mixed spinel nanocrystalline Ni−Zn−Cu-ferrite. *J. Alloys Compd.* **2009**, *473* (1), 15−19.

(30) Patoux, S.; Daniel, L.; Bourbon, C.; Lignier, H.; Pagano, C.; Le Cras, F.; Jouanneau, S.; Martinet, S. High voltage spinel oxides for Li-ion batteries: From the material research to the application. *J. Power Sources* **2009**, *189* (1), 344−352.

(31) Menini, L.; Pereira, M. C.; Parreira, L. A.; Fabris, J. D.; Gusevskaya, E. V. Cobalt- and manganese-substituted ferrites as efficient single-site heterogeneous catalysts for aerobic oxidation of monoterpenic alkenes under solvent-free conditions. *J. Catal.* **2008**, *254* (2), 355−364.

(32) Toledo-Antonio, J. A.; Nava, N.; Martínez, M.; Bokhimi, X. Correlation between the magnetism of non-stoichiometric zinc ferrites and their catalytic activity for oxidative dehydrogenation of 1-butene. *Appl. Catal., A* **2002**, *234* (1), 137−144.

(33) Rashad, M. M.; Fouad, O. A. Synthesis and characterization of nano-sized nickel ferrites from fly ash for catalytic oxidation of CO. *Mater. Chem. Phys.* **2005**, *94* (2), 365−370.

(34) Khan, A.; Smirniotis, P. G. Relationship between temperature-programmed reduction profile and activity of modified ferrite-based catalysts for WGS reaction. *J. Mol. Catal. A: Chem.* **2008**, *280* (1), 43−51.

(35) Chonco, Z. H.; Lodya, L.; Claeys, M.; van Steen, E. Copper ferrites: A model for investigating the role of copper in the dynamic iron-based Fischer−Tropsch catalyst. *J. Catal.* **2013**, *308*, 363−373.

(36) Kumar, N.; Smith, M. L.; Spivey, J. J. Characterization and testing of silica-supported cobalt−palladium catalysts for conversion of syngas to oxygenates. *J. Catal.* **2012**, *289*, 218−226.

(37) Luk, H. T.; Mondelli, C.; Ferré, D. C.; Stewart, J. A.; Pérez-Ramírez, J. Status and prospects in higher alcohols synthesis from syngas. *Chem. Soc. Rev.* **2017**, *46* (5), 1358−1426.

(38) Bengelsdorf, F. R.; Straub, M.; Dürre, P. Bacterial synthesis gas (syngas) fermentation. *Environ. Technol.* **2013**, *34* (13−14), 1639−1651.

(39) Nakagawa, Y.; Tajima, N.; Hirao, K. *J. Comput. Chem.* **2000**, *21* (14), 1292−1304.

(40) Xiang, Y.; Barbosa, R.; Kruse, N. Higher Alcohols through CO Hydrogenation over CoCu Catalysts: Influence of Precursor Activation. *ACS Catal.* **2014**, *4* (8), 2792−2800.

(41) Xiang, Y.; Kovarik, L.; Kruse, N. Rate and selectivity hysteresis during the carbon monoxide hydrogenation over promoted Co/MnO_x catalysts. *Nat. Commun.* **2019**, *10* (1), 3953.

(42) Zhao, Z.; Lu, W.; Yang, R.; Zhu, H.; Dong, W.; Sun, F.; Jiang, Z.; Lyu, Y.; Liu, T.; Du, H.; Ding, Y. Insight into the Formation of Co@Co_2C Catalysts for Direct Synthesis of Higher Alcohols and Olefins from Syngas. *ACS Catal.* **2018**, *8* (1), 228−241.

(43) Liu, Y.; Murata, K.; Inaba, M. Synthesis of mixed alcohols from synthesis gas over alkali and Fischer−Tropsch metals modified MoS_2/Al_2O_3-montmorillonite catalysts. *React. Kinet., Mech. Catal.* **2014**, *113* (1), 187−200.

(44) Wu, Q.; Christensen, J. M.; Chiarello, G. L.; Duchstein, L. D. L.; Wagner, J. B.; Temel, B.; Grunwaldt, J.-D.; Jensen, A. D. Supported molybdenum carbide for higher alcohol synthesis from syngas. *Catal. Today* **2013**, *215*, 162−168.

(45) Ojeda, M.; Granados, M. L.; Rojas, S.; Terreros, P.; García-García, F. J.; Fierro, J. L. G. Manganese-promoted Rh/Al_2O_3 for C_2-oxygenates synthesis from syngas: Effect of manganese loading. *Appl. Catal., A* **2004**, *261* (1), 47−55.

(46) Pijolat, M.; Perrichon, V. Synthesis of alcohols from CO and H_2 on a Fe/$A1_20_3$ catalyst at 8−30 bar pressure. *Appl. Catal.* **1985**, *13* (2), 321−333.

(47) Ding, M.; Ma, L.; Zhang, Q.; Wang, C.; Zhang, W.; Wang, T. Enhancement of conversion from bio-syngas to higher alcohols fuels over K-promoted Cu-Fe bimodal pore catalysts. *Fuel Process. Technol.* **2017**, *159*, 436−441.

(48) Dry, M. E. High quality diesel via the Fischer−Tropsch process − a review. *J. Chem. Technol. Biotechnol.* **2002**, *77* (1), 43−50.

(49) Arulmurugan, R.; Jeyadevan, B.; Vaidyanathan, G.; Sendhilnathan, S. Effect of zinc substitution on Co−Zn and Mn−Zn ferrite nanoparticles prepared by co-precipitation. *J. Magn. Magn. Mater.* **2005**, *288*, 470−477.

(50) Fischer, N.; Claeys, M. Phase changes studied under in situ conditions—A novel cell. *Catal. Today* **2016**, *275*, 149−154.

(51) Claeys, M. C. M.; Fischer, N. F. Sample presentation device for radiation-based analytical equipment. U.S. Patent 8,597,598 B2, 2013.

(52) Fischer, N.; Clapham, B.; Feltes, T.; van Steen, E.; Claeys, M. Size-Dependent Phase Transformation of Catalytically Active Nanoparticles Captured In Situ. *Angew. Chem., Int. Ed.* **2014**, *53* (5), 1342−1345.

(53) Claeys, M.; Dry, M. E.; van Steen, E.; du Plessis, E.; van Berge, P. J.; Saib, A. M.; Moodley, D. J. In situ magnetometer study on the formation and stability of cobalt carbide in Fischer−Tropsch synthesis. *J. Catal.* **2014**, *318*, 193−202.

(54) Claeys, M.; Van Steen, E.; Visagie, J. L.; Van de Loosdrecht, J. Magnetometer. U.S. patent 8,773,118 B2, 2014.

(55) Dalmon, J.-A. Magnetic Measurements and Catalysis. In *Catalyst Characterization: Physical Techniques for Solid Materials*; Imelik, B., Vedrine, J. C., Eds.; Springer US: Boston, MA, 1994; pp 585−609.

(56) Fischer, N.; Henkel, R.; Hettel, B.; Iglesias, M.; Schaub, G.; Claeys, M. Hydrocarbons via CO_2 Hydrogenation Over Iron Catalysts: The Effect of Potassium on Structure and Performance. *Catal. Lett.* **2016**, *146* (2), 509−517.

(57) Schulz, H.; Geertsema, A. *Erdol und Kohle* **1977**, *30*, 313−321.

(58) Wolf, M.; Fischer, N.; Claeys, M. Effectiveness of catalyst passivation techniques studied in situ with a magnetometer. *Catal. Today* **2016**, *275*, 135−140.

(59) Song, K.; Lee, Y.; Jo, M. R.; Nam, K. M.; Kang, Y.-M. Comprehensive design of carbon-encapsulated Fe_3O_4 nanocrystals and their lithium storage properties. *Nanotechnology* **2012**, *23* (50), 505401−505406.

(60) Murugappan, K.; Silvester, D. S.; Chaudhary, D.; Arrigan, D. W. M. Electrochemical Characterization of an Oleyl-coated Magnetite Nanoparticle-Modified Electrode. *ChemElectroChem* **2014**, *1* (7), 1211−1218.

(61) Shebanova, O. N.; Lazor, P. Raman spectroscopic study of magnetite ($FeFe_2O_4$): a new assignment for the vibrational spectrum. *J. Solid State Chem.* **2003**, *174* (2), 424−430.

(62) Yue-Jian, C.; Juan, T.; Fei, X.; Jia-Bi, Z.; Ning, G.; Yi-Hua, Z.; Ye, D.; Liang, G. Synthesis, self-assembly, and characterization of PEG-coated iron oxide nanoparticles as potential MRI contrast agent. *Drug Dev. Ind. Pharm.* **2010**, *36* (10), 1235−44.

(63) Graves, P. R.; Johnston, C.; Campaniello, J. J. Raman scattering in spinel structure ferrites. *Mater. Res. Bull.* **1988**, *23* (11), 1651−1660.

(64) Beattie, I. R.; Gilson, T. R. The single-crystal Raman spectra of nearly opaque materials. Iron(III) oxide and chromium(III) oxide. *J. Chem. Soc. A* **1970**, No. 0, 980−986.

(65) Coelho, A. Indexing of powder diffraction patterns by iterative use of singular value decomposition. *J. Appl. Crystallogr.* **2003**, *36* (1), 86−95.

(66) Ding, M.; Yang, Y.; Wu, B.; Li, Y.; Wang, T.; Ma, L. Study on reduction and carburization behaviors of iron phases for iron-based Fischer−Tropsch synthesis catalyst. *Appl. Energy* **2015**, *160*, 982−989.

(67) Conner, W. C.; Falconer, J. L. Spillover in Heterogeneous Catalysis. *Chem. Rev.* **1995**, *95* (3), 759−788.

(68) Nabaho, D.; Niemantsverdriet, J. W.; Claeys, M.; van Steen, E. Hydrogen spillover in the Fischer−Tropsch synthesis: An analysis of platinum as a promoter for cobalt−alumina catalysts. *Catal. Today* **2016**, *261*, 17−27.

(69) Kolhatkar, A. G.; Jamison, A. C.; Litvinov, D.; Willson, R. C.; Lee, T. R. Tuning the magnetic properties of nanoparticles. *Int. J. Mol. Sci.* **2013**, *14* (8), 15977−16009.

(70) Lee, J.-H.; Huh, Y.-M.; Jun, Y.-w.; Seo, J.-w.; Jang, J.-t.; Song, H.-T.; Kim, S.; Cho, E.-J.; Yoon, H.-G.; Suh, J.-S.; Cheon, J. Artificially engineered magnetic nanoparticles for ultra-sensitive molecular imaging. *Nat. Med.* **2007**, *13* (1), 95−99.

(71) Maaz, K.; Mumtaz, A.; Hasanain, S. K.; Ceylan, A. Synthesis and magnetic properties of cobalt ferrite ($CoFe_2O_4$) nanoparticles prepared by wet chemical route. *J. Magn. Magn. Mater.* **2007**, *308* (2), 289−295.

(72) Gong, Y. X.; Zhen, L.; Jiang, J. T.; Xu, C. Y.; Shao, W. Z. Preparation of CoFe alloy nanoparticles with tunable electromagnetic wave absorption performance. *J. Magn. Magn. Mater.* **2009**, *321* (22), 3702−3705.

(73) Nabiyouni, G; Fesharaki, M. J.; Mozafari, M; Amighian, J Characterization and Magnetic Properties of Nickel Ferrite Nanoparticles Prepared by Ball Milling Technique. *Chin. Phys. Lett.* **2010**, *27* (12), 126401−4.

(74) van Helden, P.; Prinsloo, F.; van den Berg, J.-A.; Xaba, B.; Erasmus, W.; Claeys, M.; van de Loosdrecht, J. Cobalt-nickel bimetallic Fischer−Tropsch catalysts: A combined theoretical and experimental approach. *Catal. Today* **2020**, *342*, 88−98.

(75) Dijith, K. S.; Aiswarya, R.; Praveen, M.; Pillai, S.; Surendran, K. P. Polyol derived Ni and NiFe alloys for effective shielding of electromagnetic interference. *Mater. Chem. Front.* **2018**, *2* (10), 1829−1841.

(76) Dumitru, R.; Papa, F.; Balint, I.; Culita, D. C.; Munteanu, C.; Stanica, N.; Ianculescu, A.; Diamandescu, L.; Carp, O. Mesoporous cobalt ferrite: A rival of platinum catalyst in methane combustion reaction. *Appl. Catal., A* **2013**, *467*, 178−186.

(77) Jozwiak, W. K.; Kaczmarek, E.; Maniecki, T. P.; Ignaczak, W.; Maniukiewicz, W. Reduction behavior of iron oxides in hydrogen and carbon monoxide atmospheres. *Appl. Catal., A* **2007**, *326* (1), 17−27.

(78) Braga, T. P.; Sales, B. M. C.; Pinheiro, A. N.; Herrera, W. T.; Baggio-Saitovitch, E.; Valentini, A. Catalytic properties of cobalt and nickel ferrites dispersed in mesoporous silicon oxide for ethylbenzene dehydrogenation with CO_2. *Catal. Sci. Technol.* **2011**, *1* (8), 1383−1392.

(79) Hurst, N. W.; Gentry, S. J.; Jones, A.; McNicol, B. D. Temperature Programmed Reduction. *Catal. Rev.: Sci. Eng.* **1982**, *24* (2), 233−309.

(80) Unmuth, E. E.; Schwartz, L. H.; Butt, J. B. Iron alloy Fischer−Tropsch catalysts: I: Carburization studies of the Fe-Ni system. *J. Catal.* **1980**, *63* (2), 404−414.

(81) Cheng-Hua, Z.; Yong, Y.; Zhi-Chao, T. A. O.; Hong-Wei, X.; Yong-Wang, L. I. Structural properties and reduction behavior of Ni promoted FeMnK/SiO_2 catalysts for Fischer−Tropsch synthesis. *J. Fuel Chem. Technol.* **2006**, *34* (6), 695−699.

(82) Li, S.; Li, A.; Krishnamoorthy, S.; Iglesia, E. Effects of Zn, Cu, and K Promoters on the Structure and on the Reduction, Carburization, and Catalytic Behavior of Iron-Based Fischer−Tropsch Synthesis Catalysts. *Catal. Lett.* **2001**, *77* (4), 197−205.

(83) Wu, B.; Tian, L.; Xiang, H.; Zhang, Z.; Li, Y.-W. Novel precipitated iron Fischer−Tropsch catalysts with Fe_3O_4 coexisting with α-Fe_2O_3. *Catal. Lett.* **2005**, *102* (3), 211−218.

(84) Kniess, C. T.; Lima, J. C. d.; Prates, P. B. The Quantification of Crystalline Phases in Materials: Applications of Rietveld Method. In *Sintering − Methods and Products*; Shatokha, V., Ed.; InTech: Croatia, 2012; pp 293−316.

(85) de Smit, E.; Weckhuysen, B. M. The renaissance of iron-based Fischer−Tropsch synthesis: on the multifaceted catalyst deactivation behaviour. *Chem. Soc. Rev.* **2008**, *37* (12), 2758−2781.

(86) Chen, W.; Kimpel, T. F.; Song, Y.; Chiang, F.-K.; Zijlstra, B.; Pestman, R.; Wang, P.; Hensen, E. J. M. Influence of Carbon Deposits on the Cobalt-Catalyzed Fischer−Tropsch Reaction: Evidence of a Two-Site Reaction Model. *ACS Catal.* **2018**, *8* (2), 1580−1590.

(87) Nishiyama, Y.; Tamai, Y. Deposition of carbon and its hydrogenation catalyzed by nickel. *Carbon* **1976**, *14* (1), 13−17.

(88) Pradhan, A. R.; Wu, J. F.; Jong, S. J.; Tsai, T. C.; Liu, S. B. An ex situ methodology for characterization of coke by TGA and ^{13}C CP-MAS NMR spectroscopy. *Appl. Catal., A* **1997**, *165* (1), 489−497.

(89) He, S.; Sun, C.; Yang, X.; Wang, B.; Dai, X.; Bai, Z. Characterization of coke deposited on spent catalysts for long-chain-paraffin dehydrogenation. *Chem. Eng. J.* **2010**, *163* (3), 389−394.

(90) Sahoo, S. K.; Rao, P. V. C.; Rajeshwer, D.; Krishnamurthy, K. R.; Singh, I. D. Structural characterization of coke deposits on industrial spent paraffin dehydrogenation catalysts. *Appl. Catal., A* **2003**, *244* (2), 311−321.

(91) Gopiraman, M.; Deng, D.; Ganesh Babu, S.; Hayashi, T.; Karvembu, R.; Kim, I. S. Sustainable and Versatile CuO/GNS Nanocatalyst for Highly Efficient Base Free Coupling Reactions. *ACS Sustainable Chem. Eng.* **2015**, *3* (10), 2478−2488.

(92) Gopiraman, M.; Ganesh Babu, S.; Khatri, Z.; Kai, W.; Kim, Y. A.; Endo, M.; Karvembu, R.; Kim, I. S. Dry Synthesis of Easily Tunable Nano Ruthenium Supported on Graphene: Novel Nanocatalysts for Aerial Oxidation of Alcohols and Transfer Hydrogenation of Ketones. *J. Phys. Chem. C* **2013**, *117* (45), 23582−23596.

(93) Babu, S. G.; Gopiraman, M.; Deng, D.; Wei, K.; Karvembu, R.; Kim, I. S. Robust Au−Ag/graphene bimetallic nanocatalyst for multifunctional activity with high synergism. *Chem. Eng. J.* **2016**, *300*, 146−159.

(94) Scheibe, H.-J.; Drescher, D.; Alers, P. Raman characterization of amorphous carbon films. *Fresenius' J. Anal. Chem.* **1995**, *353* (5), 695−697.

(95) Dillon, R. O.; Woollam, J. A.; Katkanant, V. Use of Raman scattering to investigate disorder and crystallite formation in as-deposited and annealed carbon films. *Phys. Rev. B: Condens. Matter Mater. Phys.* **1984**, *29* (6), 3482−3489.

(96) Dry, M. E. FT catalysts. In *Stud. Surf. Sci. Catal.*; Steynberg, A., Dry, M., Eds.; Elsevier, 2004; Vol. *152*, Chapter 7, pp 533−600.

(97) Patzlaff, J.; Liu, Y.; Graffmann, C.; Gaube, J. Studies on product distributions of iron and cobalt catalyzed Fischer−Tropsch synthesis. *Appl. Catal., A* **1999**, *186* (1), 109−119.

(98) Watanabe, K.; Miyao, T.; Higashiyama, K.; Yamashita, H.; Watanabe, M. Preparation of a mesoporous ceria−zirconia supported Ni−Fe catalyst for the high temperature water−gas shift reaction. *Catal. Commun.* **2011**, *12* (11), 976−979.

(99) Ashok, J.; Wai, M. H.; Kawi, S. Nickel-based Catalysts for High-temperature Water Gas Shift Reaction-Methane Suppression. *ChemCatChem* **2018**, *10* (18), 3927−3942.

(100) Watanabe, K.; Miyao, T.; Higashiyama, K.; Yamashita, H.; Watanabe, M. High temperature water−gas shift reaction over hollow Ni−Fe−Al oxide nano-composite catalysts prepared by the solution-spray plasma technique. *Catal. Commun.* **2009**, *10* (14), 1952−1955.

(101) Grobler, T.; Claeys, M.; van Steen, E.; Janse van Vuuren, M. J. GC × GC: A novel technique for investigating selectivity in the Fischer−Tropsch synthesis. *Catal. Commun.* **2009**, *10* (13), 1674−1680.

(102) Di Sanzo, F. P.; Lane, J. L.; Bergquist, P. M.; Mooney, S. A.; Wu, B. G. Determination of total oxygenates in fischer-tropsch liquid products. *J. Chromatogr. A* **1983**, *281*, 101−108.

(103) Anderson, R. R.; White, C. M. Analysis of Fischer−Tropsch by-product waters by gas chromatography. *J. High Resolut. Chromatogr.* **1994**, *17* (4), 245−250.

(104) Nel, R. J. J.; de Klerk, A. Fischer−Tropsch Aqueous Phase Refining by Catalytic Alcohol Dehydration. *Ind. Eng. Chem. Res.* **2007**, *46* (11), 3558−3565.

(105) Gnanamani, M. K.; Jacobs, G.; Graham, U. M.; Ribeiro, M. C.; Noronha, F. B.; Shafer, W. D.; Davis, B. H. Influence of carbide formation on oxygenates selectivity during Fischer−Tropsch synthesis over Ce-containing Co catalysts. *Catal. Today* **2016**, *261*, 40−47.

(106) Xiong, J.; Ding, Y.; Wang, T.; Yan, L.; Chen, W.; Zhu, H.; Lu, Y. The formation of Co_2C species in activated carbon supported cobalt-based catalysts and its impact on Fischer−Tropsch reaction. *Catal. Lett.* **2005**, *102* (3), 265−269.

(107) Tau, L. M.; Dabbagh, H. A.; Davis, B. H. Fischer−Tropsch synthesis: carbon-14 tracer study of alkene incorporation. *Energy Fuels* **1990**, *4* (1), 94−99.

(108) Pichler, H.; Schulz, H. *Chem. Ing. Tech.* **1970**, *42* (18), 1162−1174.

(109) Schulz, H.; Schaub, G.; Claeys, M.; Riedel, T. Transient initial kinetic regimes of Fischer−Tropsch synthesis. *Appl. Catal., A* **1999**, *186* (1), 215−227.

(110) Goldman, A. Crystal Structure of Ferrites. *Modern Ferrite Technology*, 2nd ed.; Springer US: Pittsburgh, PA, 2006; pp 51−70.

(111) Botes, F. G.; Niemantsverdriet, J. W.; van de Loosdrecht, J. A comparison of cobalt and iron based slurry phase Fischer−Tropsch synthesis. *Catal. Today* **2013**, *215*, 112−120.

(112) Schulz, H.; Claeys, M. Reactions of α-olefins of different chain length added during Fischer−Tropsch synthesis on a cobalt catalyst in a slurry reactor. *Appl. Catal., A* **1999**, *186* (1), 71−90.

(113) Iglesia, E.; Reyes, S. C.; Madon, R. J.; Soled, S. L. Selectivity Control and Catalyst Design in the Fischer−Tropsch Synthesis: Sites, Pellets, and Reactors. In *Adv. Catal.*; Eley, D. D., Pines, H., Weisz, P. B., Eds.; Academic Press, 1993; Vol. *39*, pp 221−302.

(114) Kuipers, E. W.; Scheper, C.; Wilson, J. H.; Vinkenburg, I. H.; Oosterbeek, H. Non-ASF Product Distributions Due to Secondary Reactions during Fischer−Tropsch Synthesis. *J. Catal.* **1996**, *158* (1), 288−300.

(115) Ma, W.; Kugler, E. L.; Dadyburjor, D. B. Promotional Effect of Copper on Activity and Selectivity to Hydrocarbons and Oxygenates for Fischer−Tropsch Synthesis over Potassium-Promoted Iron Catalysts Supported on Activated Carbon. *Energy Fuels* **2011**, *25* (5), 1931−1938.

(116) Zhang, X.; Liu, Y.; Liu, G.; Tao, K.; Jin, Q.; Meng, F.; Wang, D.; Tsubaki, N. Product distributions including hydrocarbon and oxygenates of Fischer−Tropsch synthesis over mesoporous MnO_2-supported Fe catalyst. *Fuel* **2012**, *92* (1), 122−129.

(117) Johnston, P.; Joyner, R. W. Structure-Function Relationships in Heterogeneous Catalysis: the Embedded Surface Molecule Approach and Its Applications. In *Stud. Surf. Sci. Catal.*; Guczi, L.; Solymosi, F.; Tétényi, P., Eds.; Elsevier, 1993; Vol. *75*, pp 165−180.

(118) Zhao, L.; Mu, X.; Liu, T.; Fang, K. Bimetallic Ni−Co catalysts supported on Mn−Al oxide for selective catalytic CO hydrogenation to higher alcohols. *Catal. Sci. Technol.* **2018**, *8* (8), 2066−2076.

(119) Davis, B. H. Fischer−Tropsch synthesis: current mechanism and futuristic needs. *Fuel Process. Technol.* **2001**, *71* (1), 157−166.

(120) Ozbek, M. O.; Niemantsverdriet, J. W. Methane, formaldehyde and methanol formation pathways from carbon monoxide

and hydrogen on the (001) surface of the iron carbide χ-Fe_5C_2. *J. Catal.* **2015**, *325*, 9−18.
(121) Spivey, J. J.; Egbebi, A. Heterogeneous catalytic synthesis of ethanol from biomass-derived syngas. *Chem. Soc. Rev.* **2007**, *36* (9), 1514−1528.
(122) Davis, B. H. Fischer−Tropsch Synthesis: Reaction mechanisms for iron catalysts. *Catal. Today* **2009**, *141* (1), 25−33.
(123) Gall, D.; Gibson, E. J.; Hall, C. C. The distribution of alcohols in the products of the Fischer−Tropsch synthesis. *J. Appl. Chem.* **1952**, *2* (7), 371−380.
(124) Schulz, H.; van Steen, E.; Claeys, M. Selectivity and mechanism of Fischer−Tropsch synthesis with iron and cobalt catalysts. In *Stud. Surf. Sci. Catal.*; Curry-Hyde, H. E., Howe, R. F., Eds.; Elsevier, 1994; Vol. *81*, pp 455−460.
(125) Ao, M.; Pham, G. H.; Sunarso, J.; Tade, M. O.; Liu, S. Active Centers of Catalysts for Higher Alcohol Synthesis from Syngas: A Review. *ACS Catal.* **2018**, *8* (8), 7025−7050.

https://dx.doi.org/10.1021/acscatal.0c03346
ACS Catal. 2020, 10, 14661−14677